Dissimilarity between dust, heat, and momentum turbulent transports during aeolian soil erosion

Sylvain Dupont, J.-L Rajot, M. Labiadh, G. Bergametti, Eric Lamaud, M. Irvine, S. Alfaro, C. Bouet, R. Fernandes, B. Khalfallah, et al.

JGR Atmospheres

RESEARCH ARTICLE
10.1029/2018JD029048

Dissimilarity Between Dust, Heat, and Momentum Turbulent Transports During Aeolian Soil Erosion

S. Dupont[1], J.-L. Rajot[2,3,4], M. Labiadh[3], G. Bergametti[4], E. Lamaud[1], M. R. Irvine[1], S. C. Alfaro[4], C. Bouet[2,4], R. Fernandes[1], B. Khalfallah[4], B. Marticorena[4], J. M. Bonnefond[1], S. Chevaillier[4], D. Garrigou[1], T. Henry-des-Tureaux[2,3], S. Sekrafi[3], and P. Zapf[4]

[1]ISPA, INRA, Bordeaux Sciences Agro, Villenave d'Ornon, France, [2]iEES Paris (Institut d'Ecologie et des Sciences de l'Environnement de Paris), UMR IRD 242, Université Paris Est Créteil-Sorbonne Université-CNRS-INRA-Université Paris Diderot, Bondy, France, [3]IRA-Médenine, Médenine, Tunisia, [4]LISA (Laboratoire Interuniversitaire des Systèmes Atmosphériques), UMR CNRS 7583, Universités Paris Est Créteil et Paris Diderot, IPSL, Créteil, France

Abstract Measuring accurately size-resolved dust flux near the surface is crucial for better quantifying dust losses by semiarid soils. Dust fluxes have been usually estimated from the flux-gradient approach, assuming similarity between dust and momentum turbulent transport. This similarity has, however, never been verified. Here we investigate the similarity between dust (0.3 to 6.0 μm in diameter), momentum, and heat fluxes during aeolian erosion events. These three fluxes were measured by the Eddy Covariance technique during the WIND-O-V (WIND erOsion in presence of sparse Vegetation's) 2017 field experiment over an isolated erodible bare plot in South Tunisia. Our measurements confirm the prevalence of ejection and sweep motions in transporting dust as for heat and momentum. However, our measurements also reveal a different partition of the dust flux between ejection and sweep motions and between eddy time scales compared to that of momentum and heat fluxes. This dissimilarity results from the intermittency of the dust emission compared to the more continuous emission (absorption) of heat (momentum) at the surface. Unlike heat emission and momentum absorption, dust release is conditioned by the wind intensity to initiate sandblasting. Consequently, ejection motions do not carry dust as often as heat and low momentum from the surface. This dissimilarity diminishes with increasing wind intensity as saltation patterns, and thus dust emission through sandblasting, become spatially more frequent. Overall, these findings may have implications on the evaluation of dust flux from techniques based on similarity with momentum or heat turbulent transport.

Key Points:
- The near-surface size-resolved dust flux is estimated using the eddy covariance technique
- Dissimilarity between dust, heat, and momentum turbulent transports is observed due to the large intermittency of the dust emission
- Our findings have implications on the evaluation of dust flux using techniques based on similarity with momentum-heat turbulent transport

Supporting Information:
- Supporting Information S1

Correspondence to:
S. Dupont,
sylvain.dupont@inra.fr

Citation:
Dupont, S., Rajot, J.-L., Labiadh, M., Bergametti, G., Lamaud, E., Irvine, M. R., et al. (2019). Dissimilarity between dust, heat, and momentum turbulent transports during aeolian soil erosion. *Journal of Geophysical Research: Atmospheres*, *124*, 1064–1089. https://doi.org/10.1029/2018JD029048

Received 22 MAY 2018
Accepted 21 DEC 2018
Accepted article online 7 JAN 2019
Published online 25 JAN 2019

1. Introduction

Aeolian soil erosion is responsible for about 32% of the annual natural mass emission of aerosols in the atmosphere (IPCC, 2013). Desert regions are the main source of mineral dust in the atmosphere, followed by semiarid regions. Mineral dust in the atmosphere has environmental and climatic implications (Mahowald, 2011; Shao, Wyrwoll, et al. 2011; Yin et al., 2002; Yu et al., 2015) as well as health impacts related to air quality deterioration and inhalation of minute particles (Bonasoni et al., 2004; Derbyshire, 2007). Compared to desert regions, semiarid regions are characterized by a mix of bare and vegetated surfaces going from grassland, crop, shrubland, to woodland, with different erodable levels. This complex arrangement of surfaces complicates the estimation of dust emission from these regions (Pierre et al., 2018).

One of the key issues for quantifying dust emission lies on estimating the near-surface dust flux. Dust production and transport within the first meters of the surface atmospheric layer is conditioned by the near-surface turbulence. While the mechanism of dust production at the surface through sandblasting (e.g., Alfaro et al., 1997; Gomes et al., 1990) and, to a lesser extent, through direct liftoff by dust devils (Neakrase et al., 2016) has been subject to several researches, the mechanism of dust turbulent transport within the first meters above the surface has received less attention. This is why dust is usually simply assumed as passive scalars (diameter lower than 20 μm), transported as the momentum by near-surface turbulence. This hypothesis is especially used when assessing dust flux using the flux-gradient relationship, assuming equivalence between momentum and dust eddy diffusivity coefficients (Gillette et al., 1972; Ishizuka et al., 2014; Nickling & Gillies, 1993; Shao, Ishizuka, et al., 2011; Sow et al., 2009).

This similarity in dust and momentum transports was justified by the assumption that both dust and momentum are carried by the same eddies. This analogy in turbulent transport between momentum and scalars is often referred to as the Reynolds analogy (Li & Bou-Zeid, 2011). The specific eddies responsible for momentum and scalar transport are known as coherent eddy structures (Robinson, 1991). Such structures have a certain coherence in space and time compared to the random background turbulence. In near-neutral conditions such as during a synoptic-scale dust storm, turbulence is mostly shear-driven. Here the coherent structures in the near-surface layer include different nested structures (e.g., Adrian, 2007; Hutchins et al., 2012): (1) very large-scale elongated structures scaling with the boundary layer thickness and corresponding to juxtaposed meandering regions of low- and high-speed streaks, (2) inclined hairpin vortices arranged into packets resulting from the ejection of low speed from the surface, and (3) local sweeps and ejections constituting the primary motions of hairpin vortices. These last two motions, sweeps and ejections, are responsible for most of the turbulent transport of momentum and scalars in the near-surface boundary layer (e.g., Katul et al., 1997). The importance of ejections and sweeps in moving particles such as dust, away and toward the surface, respectively, has been demonstrated from Direct Numerical Simulations (e.g., Vinkovic et al., 2011) but has never been verified from field experiment.

Heat also has long been considered as transported as momentum under the same argument as for dust that both momentum and heat are carried by the same eddies. However, many studies observed a dissimilarity between heat and momentum turbulent transport, in particular with increasing instability conditions (Dupont & Patton, 2012; Li & Bou-Zeid, 2011). This dissimilarity results from the enhancement of buoyancy-driven turbulence (buoyant-thermal motions) with increasing instability and consequently the reduction of shear-driven turbulence, the former turbulence type optimizing heat transport (Li & Bou-Zeid, 2011; Salesky et al., 2017). The turbulent Prandtl number, which characterizes the ratio of turbulent diffusivities between momentum and heat, is thus often lower than one and increases with stability (Businger et al., 1971; Kays, 1994). This means that heat is transported by turbulence more efficiently than momentum, even in near-neutral conditions, although the Prandtl number exhibits large scatter for this stability condition. Similarly, differences in transport between heat and gas such as water vapor or CO_2 have also been reported due mainly to difference in distribution of sources and sinks between these scalars as well as due to the scalar gradient across the top of the boundary layer's entrainment zone, especially in convective conditions (e.g., Cava et al., 2008; Dupont & Patton, 2012; Katul et al., 2008; Lamaud & Irvine, 2006; Moene et al., 2006; Williams et al., 2007). There are therefore reasonable arguments to challenge the assumption that dust turbulent transport is in analogy to that of momentum and heat.

Dissimilarity in atmospheric turbulent transport between particles in general and momentum or heat has been less investigated. This is partly due to the difficulty of measuring directly particle fluxes using the eddy covariance technique as it requires to measure simultaneously high-frequency wind velocity components and particle concentration. Most studies having measured particle flux from this technique focused on the quantification of the flux itself and not on its analogy with momentum or heat fluxes. These studies were mainly performed over urban areas (Deventer, El-Madany, et al., 2015; Dorsey et al., 2002; Mårtensson et al., 2006), vegetated surfaces (Damay et al., 2009; Deventer, Held, et al., 2015), and much less over desert areas (Fratini et al., 2007; Porch & Gillette, 1977). The only studies comparing particle and heat turbulent transports either observed similarity between both scalars (Fratini et al., 2007; Mårtensson et al., 2006) or assumed similarity to correct their particle flux from the heat flux due to the slow response time of their particle counter (Damay et al., 2009; Deventer, Held, et al., 2015). Hence, in these studies particles are usually considered as passive scalars with the same source/sink distributions as heat. With increasing particle size, particle inertia and gravity cannot be neglected, and dissimilarity with momentum and heat is expected as particle trajectories do not follow exactly the carrier eddy (Fratini et al., 2007; Shao, 2008). These inertia and gravity effects are neglected for dust particles smaller than 10 μm in diameter (Fratini et al., 2007; Shao, 2008).

To our knowledge, only two field experiments measured dust flux by the eddy covariance technique and compared the turbulent transport of dust with that of momentum or heat. First, Porch and Gillette (1977) observed similarity between dust and momentum turbulent exchange coefficients (eddy diffusivity coefficients). Their result was, however, limited to a dust deposition period. More recently, Fratini et al. (2007) observed under strong wind conditions (friction velocity around 0.60 ms^{-1}) that dust particles (0.26–7.00-μm diameter range) act as a passive scalar and are transported as heat. This similarity between dust and heat was less verified under low wind conditions (friction velocity around 0.40 ms^{-1}); this was attributed by

Fratini et al. (2007) to an underestimation of the dust concentration due to dilution performed by their counter system. Their measurements were performed far from the surface (12 m) as compared to usual dust flux measurement height (only a few meter height), and above an extended desert region of northern China, as opposed to isolated erodible plots in semiarid regions.

We argue here that dissimilarity in turbulent transport between dust and momentum (and heat) is possible near the surface as observed for gas because of the different physics in source/sink between dust and momentum (and heat). Indeed, the absorption (emission) of momentum (heat) at the surface is dominated by convective turbulent transport, while the emission of dust is conditioned by the breakage of cohesion forces of dust particles on soil aggregates by impaction of saltating particles (sandblasting) and, less common, through direct lift force from strong wind gusts. If this dissimilarity exists, it should be accounted for in parametrizations and estimations of dust fluxes in, respectively, models and field measurements using the flux-gradient relationship. The goal of this study is to verify this dissimilarity between dust, heat, and momentum fluxes in the near-surface atmospheric layer (3-m height) during the wind erosion of an isolated bare plot in a fragmented cultural landscape, typical of semiarid regions. To that purpose, a novel field experiment was performed in South Tunisia under the research program WIND-O-V (WIND erOsion in presence of sparse Vegetation) (Dupont et al., 2018). During this experiment, wind velocity components, air temperature, and size-resolved dust concentration were measured simultaneously at high frequency at 3-m height over a flat bare soil under soil erosion conditions. The turbulent transports of momentum, heat, and dust are compared from quadrant, octant, cospectral, and multiresolution analyses.

2. The WIND-O-V's 2017 Experiment

2.1. Site

The WIND-O-V's 2017 experiment took place from 1 March to 15 May 2017 in South Tunisia, in the experimental range (Dar Dhaoui) of the Institut des Régions Arides of Médenine close to Médenine/Zarzis (Figures 1a and 1b). The site approximates a flat half-circle plot of 150-m radius where measurements were performed at the center of the circle in order to ensure a fetch of at least 150 m for westerly, northerly to easterly winds (Figure 1c). In the north, the fetch was slightly longer, about 200 m. The ground surface was flat (slope less than 0.3° in all directions). The plot was surrounded by less erodible plots with small bushes in the northwest (0.34 ± 0.08 m height and 0.58 ± 0.20 m diameter) and young olive trees arranged in a square pattern (about 1.7 ± 0.3 m height, 1.5 ± 0.4 m diameter, and 26 m spaced) in the northeast. The soil is typical of the Jeffara basin with a surface loamy sand layer very prone to wind erosion. Before the experiment and after the main rainfall events, the surface had been tilled with a disc plow and leveled with a wood board in order to meet the conditions of an ideal flat bare soil without soil crust nor ridges.

2.2. Measurements

A 9-m-high lattice mast was erected at the center of the half-circle plot (Figure 1d). On this mast, turbulent velocity components and air temperature fluctuations were measured simultaneously at 1.0, 1.9, 3.0, and 4.1 m above the surface using four 3-D ultrasonic anemometers (one Campbell Scientific CSAT3, two Gill R3, and one Gill WindMaster) sampling at 60, 50, 50, and 20 Hz, respectively. On the same mast, seven cup anemometers (0.2, 0.6, 1.3, 1.8, 3.0, 4.0, and 5.2 m) and four thermocouples (0.4, 1.6, 3.7, and 5.0 m) were also installed to measure simultaneously at 0.1 Hz the mean horizontal wind velocity and temperature profiles, respectively. All anemometers on the tower were intercalibrated prior to the experiment.

Airborne dust concentration per size class was measured at 1 Hz from three PALAS WELAS-2300 particle spectrometers, covering 0.3–17-μm diameter range particles and with 16 intervals per decade. The spectrometers determined the size and number of particles in sampled air in the optical chamber, delivered by a pump with a flow rate of 5 L/min. Before the experiment, the spectrometers were calibrated from monodisperse dust particles of silicon dioxide (1.28 μm in diameter) as recommended by the manufacturer. Equivalence between the refractive indices of silicon dioxide and mineral dust particles was assumed. One of the spectrometers was coupled to the 3-m height sonic anemometer in order to deduce size-resolved number dust fluxes using the eddy covariance technique. A specific small sampling head was built for this particle spectrometer in order to not disturb the measurements of the 3-m-height anemometer. This head was simply constituted of a 25-cm-long and 1-cm-diameter tube with a drilled cover letting particles entering while protecting from the rain (see Figure 1e). This sampling head was positioned about 20 cm south from the head of the sonic anemometer. This head was made in order to minimize disruption of the air while sampling dust particle within the air. The two other spectrometers were used stand-alone at 2- and 4-m height

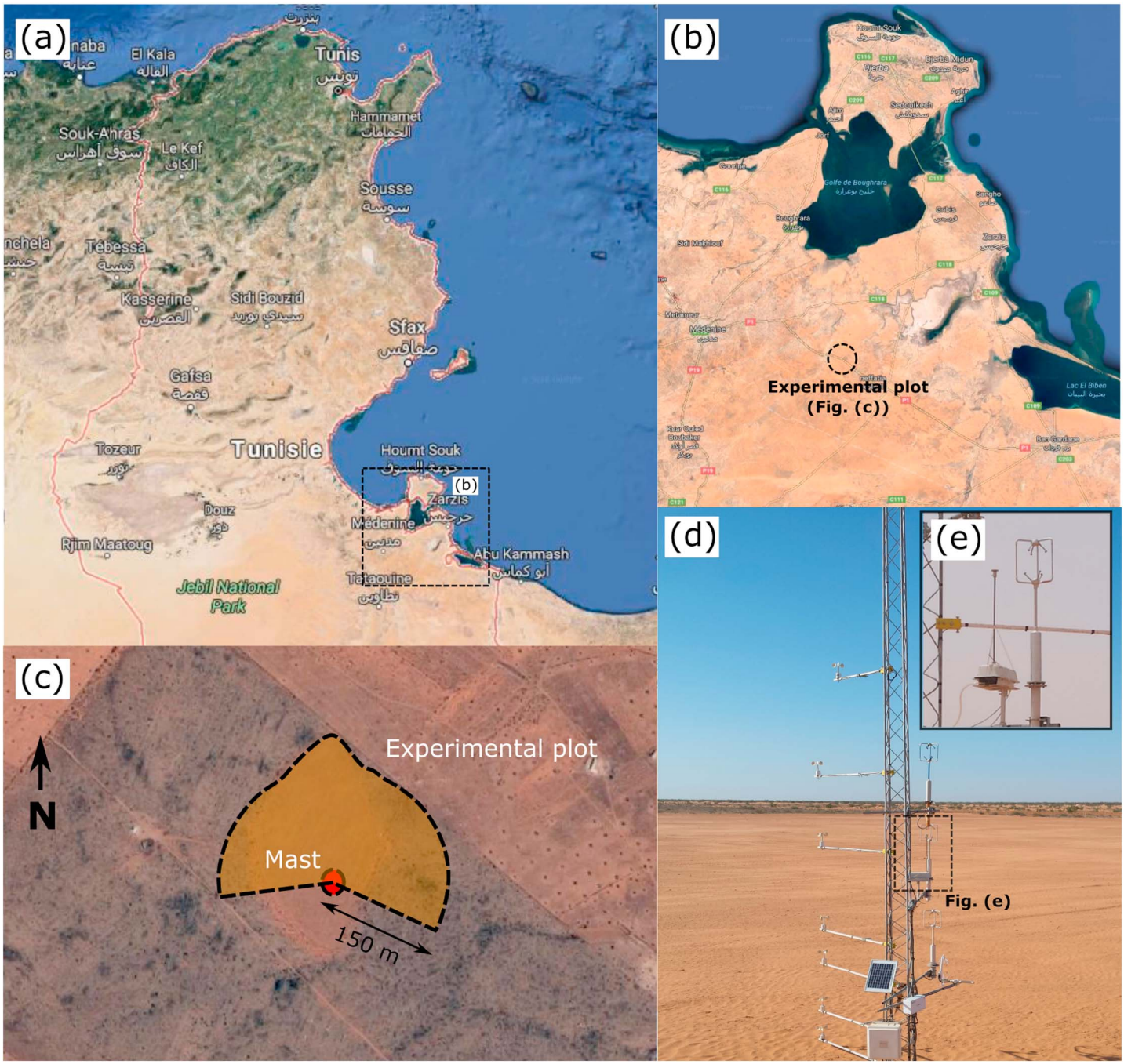

Figure 1. WIND-O-V (WIND erOsion in presence of sparse Vegetation's) 2017 experimental site. (a and b) Localization of the site in Tunisia (Google Map). (c) Schematic representation of the near-half-circle experimental plot where the measurement mast was located at its center. (d) North view of the plot from the back of the mast where cup and ultrasonic anemometers were mounted. (e) Sampling head of the particle spectrometer located downwind the 3-m-height ultrasonic anemometer.

on an other mast. Since these two spectrometers were not coupled to a sonic anemometer, they could be equipped with a standard Total Suspended Particles sampling head (BGI by Mesa Labs, Butler, NJ, United States). The particle size distribution measured by the three spectrometers was similar for particles smaller than 4 μm, confirming the negligible impact of the sampling head for such particle size range. Above 4 μm, the spectrometer equipped with the small sampling head started to underestimate the number of particles as compared to the two other spectrometers. Nonetheless, the dust concentration fluctuations of particles larger than 4 μm could still be considered valid for estimating the dust flux by eddy covariance provided

that the dust spectra still respond to the expected shape. For this study, we focus solely on data from the spectrometer coupled to the sonic anemometer.

Saltation was also followed from two Saltiphones (Eijkelkamp®, Giesbeek, the Netherlands) positioned close to the surface and several sediment traps like Big Spring Number Eight (BSNE) (Fryrear, 1986), allowing to characterize the erosion dynamics and to quantify the saltation flux and particle size distribution, respectively (see Dupont et al., 2018).

Data from all anemometers and particle spectrometers were acquired and stored simultaneously from several synchronized Raspberry Pi's assembled in a local network.

2.3. Data Processing

A 15-min averaging time was chosen for computing all statistics characterizing the wind and dust dynamics. This value was deduced in Dupont et al. (2018) from an ogive analysis, which consists in searching for the point of convergence of the cumulative momentum cospectrum to an asymptote (e.g., Oncley et al., 1996). This averaging time ensures that all significant turbulent structures carrying momentum flux, and thus other fluxes, are included in the statistics. On each 15-min period, a Reynolds decomposition was applied to all variables of interest such as wind velocity components, air temperature, or dust concentration. Hence, a variable α was decomposed into $\alpha = \langle\alpha\rangle + \alpha'$, where the symbol $\langle\rangle$ denotes the time average and the prime the deviation from the averaged value. Prior to this decomposition, the large-scale trend on α with period larger than 15 min was simply removed from a sixth-order polynomial fit.

The wind velocity components recorded from the sonic anemometers were rotated horizontally so that u represents the horizontal component along the mean wind direction x and v the horizontal component along the transverse direction y. In order to account for possible errors in the vertical orientation of the sonic anemometers, a second rotation was performed at every height around the y axis.

Dust concentration fluctuations were compared-correlated with the fluctuations of the wind velocity components reduced to the frequency of the particle spectrometer (1 Hz). A time-lag correction was applied on the dust fluctuations for each averaging time (15 min). This time lag was deduced by maximizing the covariance between the dust concentration and vertical wind velocity fluctuations. Overall, this time lag remained small, varying between −1 and +2 s, as the dust sensor was very close to the sonic anemometer. To simplify the analysis, size-resolved dust concentration was also synthesized in seven bins between 0.3 and 17 μm by aggregating by four the intervals of the particle spectrometer and by removing the first interval, which is insufficiently accurate following the spectrometer constructor.

Quality controls of turbulence and particle measurements were performed. In particular, flow steadiness was tested for each 15-min period using the criterion given by Foken et al. (2004) in order to verify the low impact of mesoscale variability on the 15-min averaging periods. This steadiness test was not applied to dust concentration due to the intermittency of the time series (see section 4.1). This apparent nonstationarity of dust concentration was not related to mesoscale variability nor to nonphysical extreme values (spikes) but to the intermittent nature of dust emission. Since dust emission depends on wind turbulence, we considered that a 15-min averaging time was a good compromise to apply Reynolds decomposition as the flow is stationary at this scale and as all significant turbulent structures carrying flux are included in the statistics at this scale. Finally, the time series were also visualized in order to detect occasional instruments failures.

2.4. Erosion Events

Two well-defined erosion events occurred during the experiment (9 March and 20 April events), with constant mean wind direction, high wind speed, and significant levels of dust concentration in the air during several hours. Other events occurred with less ideal characteristics in term of dust concentration magnitude, wind direction constancy, or erosion duration (7 and 8 March and 14 and 16 April events). These events were, however, included in our study in order to support the findings deduced from the two main events (9 March and 20 April). Note that the 14–15 March event presented in Dupont et al. (2018) was not considered in this study as the particle spectrometer coupled to the sonic anemometer was not working during this event. Overall, this study will, therefore, focus on six events.

The main meteorological and dust concentration characteristics of these six events are presented in Figure 2. All events occurred during daytime; they are thus mainly located on the convective side of the near-neutral stability conditions ($-0.2 < z/L < 0.01$, as defined in Dupont et al., 2018; Figure 2d). The events exhibit

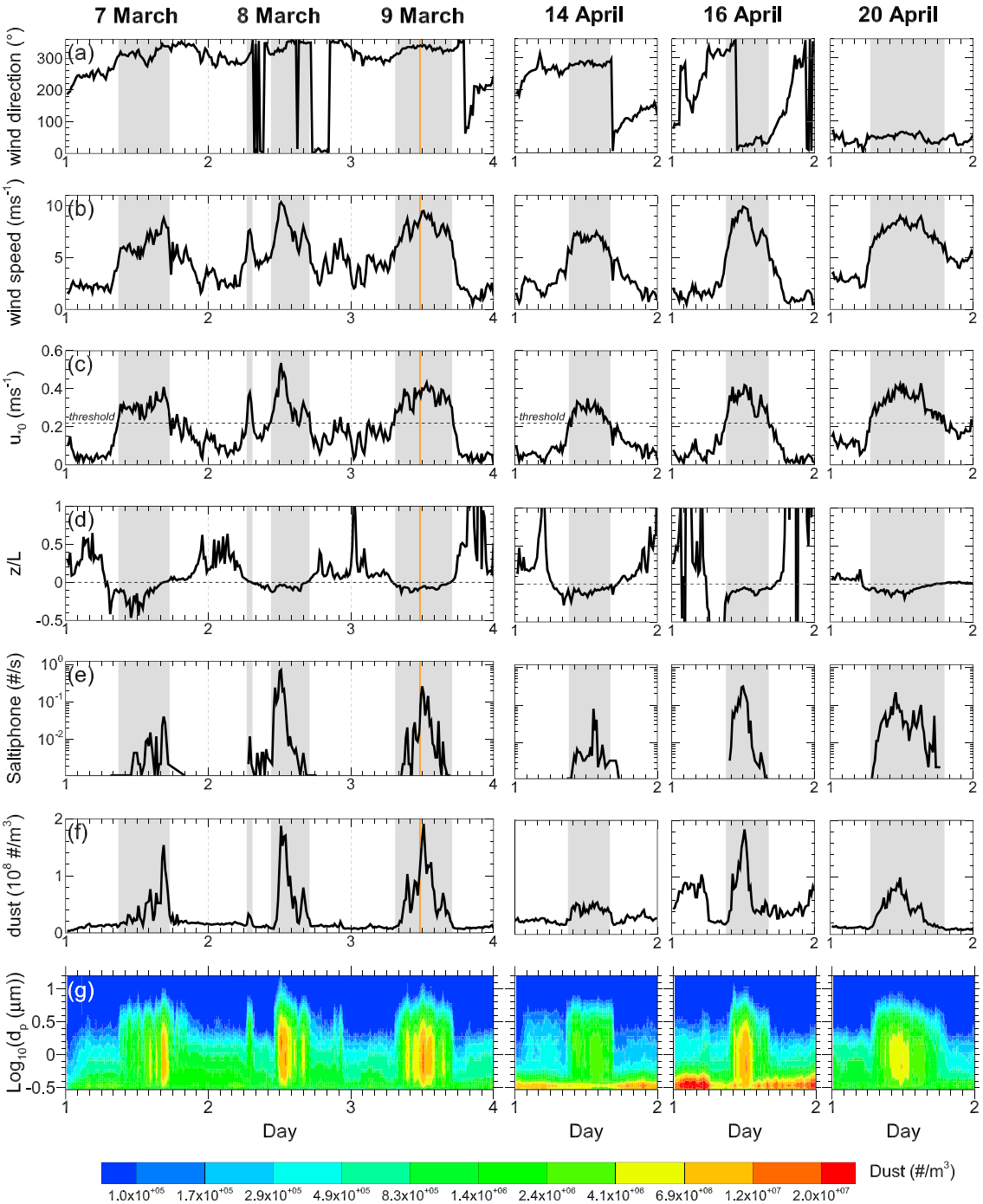

Figure 2. Main characteristics of the six erosion events: time variations of the (a) mean wind direction, (b) mean wind speed at 3-m height, (c) surface friction velocity (u_{*0}) deduced from the sonic anemometers according to Dupont et al. (2018), (d) stability, (e) mean impact number of saltating particles recorded by one of the Saltiphone, (f) total mean dust concentration in number measured at 3-m height, and (g) mean size-resolved dust concentration in number. The shaded areas highlight the erosion periods defined as $u_{*0} \geq 0.22\,\mathrm{ms}^{-1}$, where $0.22\,\mathrm{ms}^{-1}$ is the threshold friction velocity deduced in Dupont et al. (2018). The orange vertical line indicates the position of the time series presented in Figure 4.

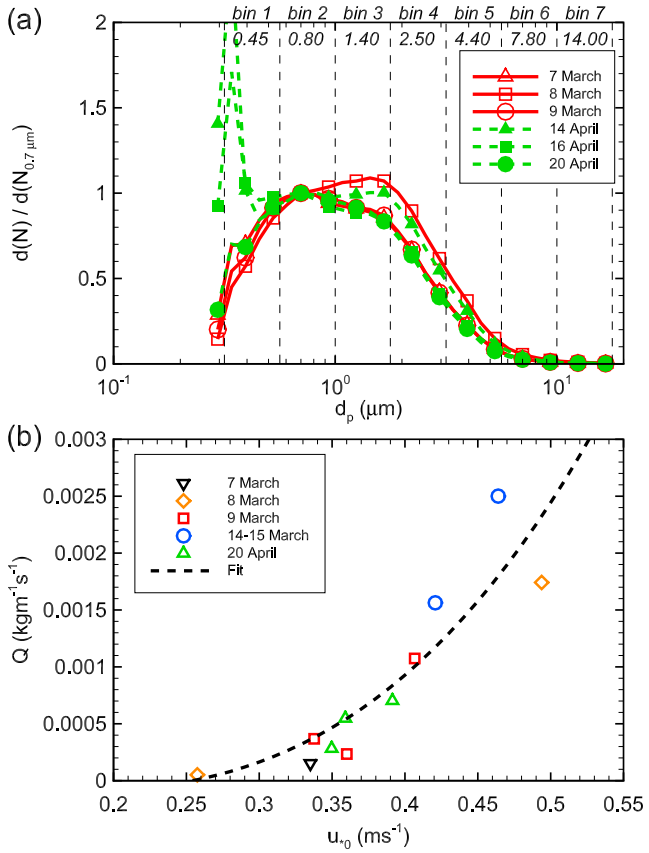

Figure 3. (a) Ensemble-averaged size-resolved dust concentration in number measured by the spectrometer at 3-m height during the six erosion events and normalized by the 0.7-μm dust concentration. The seven bins considered in our analysis are indicated with their mean particle size. (b) Saltation flux Q against the surface friction velocity (u_{*0}) obtained for the 7–9 March, 14 and 15 March, and 20 April events. The fitted curve in (b) corresponds to the parameterization of Lettau and Lettau (1978) with $c = 0.7$ (see Dupont et al., 2018). The saltation flux was not measured during the 14 and 16 April events. The 14 and 15 March event was not considered in this study (see section 2.4).

different wind directions (Figure 2a): west for the 14 April event, northwest for the 7–9 March events, and northeast for the 16 and 20 April events. During the 16 April event, the wind turned from north to northeast. The 7 March and 14 April events exhibit the lowest wind intensity (Figure 2b), and thus, the highest convective conditions and the lowest dust concentration (Figures 2f and 2g). The 8 March event presents the strongest wind peak, followed by the 16 April event. The 9 March and 20 April events exhibit similar wind intensities. Importantly, an intense rain event occurred between 9 and 10 April, before the three April wind events, with a cumulated rain of about 30 mm. This rain event formed a small surface crust that was weakened on 19 April by the passage of a wood board on the surface.

As expected, the number of impacting saltating particles recorded by the Saltiphone (Figure 2e) and the size-resolved particle number concentration measured by the particle spectrometer (Figure 2f) vary both as the wind speed (Figure 2b) for surface friction velocity u_{*0} higher than the threshold friction velocity (0.22 ms^{-1} as deduced in Dupont et al., 2018; Figure 2c). Hence, particles detected by the spectrometer are most likely mineral dust resulting from wind erosion. From now on, when performing ensemble average at the event scale, only 15-min periods with $u_{*0} \geq 0.30\ ms^{-1}$ will be considered in order to account only for well-established erosion periods.

During erosion events, the size range of particles detected by the spectrometer increased from a background concentration (Figure 2g). The mean size-resolved dust number concentrations measured by the particle spectrometer exhibit a similar distribution for all events, with a maximum around 0.7 μm, except for the strongest event (8 March event) and, in a lesser extent, for the 14 April event, where a peak around 1.7 μm is visible (Figure 3a). Note that the large peaks around 0.3 μm for the 14 and 16 April events are more likely related to air pollution than dust particles. During both days, a large concentration of particles smaller than about 0.7 μm was always present, even without dust erosion (Figure 2g). Interestingly, the dust number concentration during the 20 April event is lower than during the 9 March event, while both events had similar surface friction velocities and saltation fluxes (Figures 2c and 3b).

The wind dynamics of 7–9 March and 20 April events were previously analyzed in Dupont et al. (2018). The wind was found consistent with usual observations in surface boundary layer in terms of mean turbulent velocity profiles and main turbulent structures. This was also verified for the 14 and 16 April events (result not shown). A slight increase of the momentum flux at the top of the profile (4-m height) during the 20 April event was observed. We suspected that it was due to the shorter fetch of our experimental site for northeasterly winds compared to the northwesterly winds of the 7–9 March event. For northeasterly winds, the top of the profile was possibly contaminated by turbulence established with the rougher upwind surface outside the plot, although the mean velocity profile was well approximated by a logarithmic function. During the 14 and 16 April events, the 4-m-height level may have also been contaminated by turbulence established with the surface outside the plot due to shorter fetch for westerly and northeasterly winds, respectively (results not shown). Nevertheless, this shorter fetch for westerly and northeasterly winds is unlikely to impact our results here as our analysis focuses exclusively on measurements performed at 3-m height.

3. Method for Analyzing Similarity in Turbulent Transport

Different methods exist to investigate the similarity between the transport of quantities such as momentum, heat, and scalar (dust here), with different assumptions and different degree of details. The most general approach looks at the correlation between quantities, integrating all motion frequencies present in the time

series (correlation coefficient), while the most detailed approaches look at the flux partition according to the type (quadrant-octant analysis), the frequency (Fourier spectral analysis), or the scale (wavelet analysis) of turbulent structures composing the signal. All four methods will be used here and are detailed below. The wavelet approach used in this study is based on the Haar multiresolution flux decomposition (Howell & Mahrt, 1997).

3.1. Correlation Coefficients

Correlation coefficients between variables or fluxes represent a first simple approach to look at the similarity between quantities transported by the turbulent flow by integrating the whole frequency range of eddies. The correlation coefficient $r_{\alpha,\beta}$ between quantities α and β is defined as

$$r_{\alpha,\beta} = \frac{\langle (\alpha - \langle \alpha \rangle)\ (\beta - \langle \beta \rangle) \rangle}{\sigma_\alpha\ \sigma_\beta}, \tag{1}$$

where α and β are either the streamwise or vertical wind velocity components (u and w), air temperature (θ), dust concentration (d), momentum flux (uw), heat flux ($w\theta$), or dust flux (wd), and σ_α and σ_β are the standard deviations of α and β, respectively.

3.2. Quadrant Analysis

The quadrant analysis highlights turbulent structures associated with the complete flow (no time scale decomposition) at a specific time. The turbulent flux $\langle \alpha' \beta' \rangle$ is split into four quadrants depending on the sign of the fluctuations α' and β', irrespective of their duration or frequency. Here β is either w or u for vertical or horizontal fluxes, respectively. For simplicity when discussing the quadrants, we will refer to them as Q1, Q2, Q3, and Q4.

The flux $\langle \alpha' \beta' \rangle$ is decomposed such as $\langle \alpha' \beta' \rangle = \sum_{Qi} \langle \alpha' \beta' \rangle_{Qi}$, where $\langle \alpha' \beta' \rangle_{Qi}$ is the magnitude of the flux in quadrant Qi. Similarly, the number of events responsible for the flux is decomposed such as $n^{\alpha\beta} = \sum_{Qi} n^{\alpha\beta}_{Qi}$, where $n^{\alpha\beta}$ is the total number of events (here the number of points of the time series) and $n^{\alpha\beta}_{Qi}$ is the number of events in quadrant Qi contributing to the flux.

The magnitude percentage of the flux within quadrant Qi is computed as

$$F^{\alpha\beta}_{Qi} = 100 \times \left| \langle \alpha' \beta' \rangle_{Qi} \right| \Big/ \sum_{Qi} \left| \langle \alpha' \beta' \rangle_{Qi} \right|, \tag{2}$$

and the event number percentage within quadrant Qi is computed as

$$N^{\alpha\beta}_{Qi} = 100 \times n^{\alpha\beta}_{Qi} / n^{\alpha\beta}. \tag{3}$$

Similarity between fluxes will be characterized by a similar distribution of the flux between quadrants.

The criteria defining each of the four quadrants are presented in Table 1. For the momentum flux ($\langle u'w' \rangle$), Q1 and Q3 correspond to uw-ejection ($u' < 0$ and $w' > 0$) and uw-sweep ($u' > 0$ and $w' < 0$) motions, that is, slow momentum fluid transported upward and fast momentum fluid transported downward, respectively. For the heat flux ($\langle w'\theta' \rangle$), Q1 and Q3 events refer to as $w\theta$ ejections and $w\theta$ sweeps (warm upward and cool downward plumes, respectively) since most of erosion events occurred during daytime (positive heat flux coming from the surface). For the dust flux ($\langle w'd' \rangle$), Q1 and Q3 events refer to as wd ejections and wd sweeps (dusty upward [emission] and clean downward plumes, respectively).

3.3. Octant Analysis

In an octant analysis, the quadrant decomposition of the momentum flux is further decomposed following the sign of the temperature or scalar fluctuations in order to establish whether temperature and scalar are transported similarly as momentum (Dupont & Patton, 2012). Hence, the momentum flux in quadrant Qi ($\langle u'w' \rangle_{Qi}$) can be decomposed as

$$\langle u'w' \rangle_{Qi} = \langle u'w' \rangle^{\varphi^+}_{Qi} + \langle u'w' \rangle^{\varphi^-}_{Qi}, \tag{4}$$

and the number of events responsible for the flux is decomposed as

Table 1
Mean Fraction Values, in Event Number and in Magnitude, of the Momentum ($\langle u'w' \rangle$), Heat ($\langle w'\theta' \rangle$), and Number Size-Resolved Dust ($\langle w'd' \rangle$) Fluxes in Each Quadrant as Defined in Equations (2) and (3), Respectively, for the 9 March and 20 April Events

	9 March				20 April			
	Q1	Q2	Q3	Q4	Q1	Q2	Q3	Q4
	Ejection		Sweep		Ejection		Sweep	
	$w'+, u'-$	$w'+, u'+$	$w'-, u'+$	$w'-, u'-$	$w'+, u'-$	$w'+, u'+$	$w'-, u'+$	$w'-, u'-$
	$w'+, \theta'+$	$w'+, \theta'-$	$w'-, \theta'-$	$w'-, \theta'+$	$w'+, \theta'+$	$w'+, \theta'-$	$w'-, \theta'-$	$w'-, \theta'+$
	$w'+, d'+$	$w'+, d'-$	$w'-, d'-$	$w'-, d'+$	$w'+, d'+$	$w'+, d'-$	$w'-, d'-$	$w'-, d'+$
In number								
N_{Qi}^{uw}	0.32	0.17	0.32	0.19	0.31	0.17	0.32	0.20
$N_{Qi}^{w\theta}$	0.31	0.18	0.35	0.16	0.32	0.17	0.36	0.15
N_{Qi}^{wd} (0.45 μm)	0.23	0.26	0.37	0.14	0.24	0.25	0.36	0.15
N_{Qi}^{wd} (0.80 μm)	0.23	0.26	0.39	0.12	0.24	0.25	0.39	0.12
N_{Qi}^{wd} (1.40 μm)	0.24	0.25	0.39	0.12	0.24	0.25	0.40	0.11
N_{Qi}^{wd} (2.50 μm)	0.24	0.25	0.39	0.12	0.23	0.25	0.40	0.12
N_{Qi}^{wd} (4.40 μm)	0.23	0.27	0.38	0.12	0.21	0.28	0.39	0.12
N_{Qi}^{wd} (7.80 μm)	0.10	0.39	0.44	0.07	0.07	0.41	0.47	0.05
N_{Qi}^{wd} (14.00 μm)	0.02	0.47	0.49	0.02	0.02	0.47	0.49	0.02
In magnitude								
F_{Qi}^{uw}	0.41	0.11	0.36	0.12	0.41	0.11	0.36	0.12
$F_{Qi}^{w\theta}$	0.46	0.09	0.36	0.09	0.48	0.07	0.37	0.08
F_{Qi}^{wd} (0.45 μm)	0.46	0.14	0.29	0.11	0.45	0.14	0.29	0.12
F_{Qi}^{wd} (0.80 μm)	0.49	0.12	0.30	0.09	0.49	0.12	0.30	0.09
F_{Qi}^{wd} (1.40 μm)	0.49	0.12	0.30	0.09	0.49	0.12	0.30	0.09
F_{Qi}^{wd} (2.50 μm)	0.49	0.12	0.30	0.09	0.49	0.12	0.30	0.09
F_{Qi}^{wd} (4.40 μm)	0.45	0.15	0.29	0.11	0.45	0.16	0.28	0.11
F_{Qi}^{wd} (7.80 μm)	0.39	0.21	0.25	0.15	0.38	0.22	0.24	0.16
F_{Qi}^{wd} (14.00 μm)	0.34	0.23	0.23	0.20	0.32	0.24	0.24	0.20

$$n_{Qi}^{uw} = n_{Qi}^{uw|\varphi^+} + n_{Qi}^{uw|\varphi^-}, \tag{5}$$

where φ is either θ or d, and $^{\varphi^+}$ or $^{\varphi^-}$ refers to whether the instantaneous momentum flux coincides with positive or negative φ fluctuations.

The magnitude percentages of momentum flux in quadrant Qi coincident with positive and negative φ fluctuations are calculated using

$$F_{Qi}^{uw|\varphi^+} = 100 \times \left| \langle u'w' \rangle_{Qi}^{\varphi^+} \right| \Big/ \sum_{Qi} \left| \langle u'w' \rangle_{Qi} \right|, \tag{6}$$

and

$$F_{Qi}^{uw|\varphi^-} = 100 \times \left| \langle u'w' \rangle_{Qi}^{\varphi^-} \right| \Big/ \sum_{Qi} \left| \langle u'w' \rangle_{Qi} \right|, \tag{7}$$

and the event number percentage of momentum flux in quadrant Qi coincident with positive and negative φ fluctuations are calculated using

$$N_{Qi}^{uw|\varphi^+} = 100 \times n_{Qi}^{uw|\varphi^+} / n^{\alpha\beta}, \tag{8}$$

and

$$N_{Qi}^{uw|\varphi^-} = 100 \times n_{Qi}^{uw|\varphi^-} / n^{\alpha\beta}. \quad (9)$$

3.4. Fourier Spectral Analysis

The Fourier analysis provides information on the partition of the variance of α or of the flux $\langle \beta'\alpha' \rangle$ (β is either u or w) following the frequency of the turbulent structures. The Fourier analysis presumes that the flow is composed of a superposition of periodic turbulent structures with specific frequencies that can be separated one from the other. Hence, a time series $\alpha(k)$ over a time period T is decomposed into a finite number of sine and cosine terms such as

$$\alpha(k) = \sum_{n=0}^{N-1} \frac{S_\alpha(n)}{N} \exp(i2\pi nk/N), \quad (10)$$

where $k = t/\Delta t$ with t the time and Δt the time step, n is the number of cycles per time period T, N the number of data points ($T/\Delta t$), and $S_\alpha(n)$ the discrete Fourier transform. The portion of the signal variance explained by waves of frequency $f = n/T$ is represented by $|S_\alpha(n)|^2$. Hence, the total variance is $\sigma_\alpha^2 = \sum_{n=1}^{N-1} |S_\alpha(n)|^2$ (Stull, 1988).

Similarly, the flux $\langle \beta'\alpha' \rangle$ can be decomposed following turbulent structure frequency such as $\langle \beta'\alpha' \rangle = \sum_{n=1}^{N-1} S_\alpha(n)^* \cdot S_\beta(n)$, where $S_\alpha(n)^*$ is the complex conjugate of $S_\alpha(n)$ and $S_\alpha(n)^* \cdot S_\beta(n)$ represents the portion of the flux explained by waves of frequency f. Similarity between the turbulent transport of two quantities α will be characterized by the same distribution of their fluxes $\langle \beta'\alpha' \rangle$ according to the frequency.

3.5. MRD

The multiresolution decomposition (MRD) represents a simple discrete orthogonal decomposition of a signal or a flux, providing information on the eddy scale responsible for the signal fluctuations or for the flux. Unlike the Fourier decomposition, MRD satisfies Reynold's averaging at all scales and does not assume periodicity (Howell & Mahrt, 1997; Vickers & Mahrt, 2003). Hence, turbulent structures are defined in time as opposed to in frequency with the Fourier spectral analysis.

MRD consists in partitioning a time series $\alpha(t)$ of 2^M points into simple block averages on different scales m of dyadic width 2^m, starting from $m = M$ to $m = 0$. Hence, the first partition corresponds to the largest scale 2^M and is the simple average of α, which is then removed from the initial signal. The second partition averages the two halves of the residual signal resulting from the first partition, which are then removed, and so on (Vickers & Mahrt, 2003). The α mean value at scale m and for the nth segment is given by

$$\overline{\alpha_n}(m) = \frac{1}{2^m} \sum_{i=(n-1)2^m+1}^{n2^m} \alpha r_i(m), \quad (11)$$

where $\alpha r_i(m)$ is the signal residual after removing the block averages from scales greater than 2^m points. The number of segment at scale m is 2^{M-m}, and the length of the segments is 2^m. Nilsson et al. (2014) interpreted $\overline{\alpha_n}(m)$ as the eddy fluctuation of α at scale m from the average at scale $m+1$, calculated from the 2^m points belonging to segment n of the α time series (2^M points).

Nilsson et al. (2014) introduced the mapped time series $\overline{\alpha}(k,m)$ which consists of mapping $\overline{\alpha_n}(m)$ on the 2^M grid points of the α time series. Hence, the α time series is the sum over all scales of the mapped time series:

$$\alpha(k) = \sum_m \overline{\alpha}(k,m). \quad (12)$$

The value of the MRD spectrum (D_α) at scale $m+1$ is simply the variance of the mapped signal $\overline{\alpha}(t,m)$ at scale m:

$$D_\alpha(m+1) = \frac{1}{2^M} \sum_{k=1}^{2^M} \overline{\alpha}^2(k,m), \quad (13)$$

where the sum of D_α on all scales is equal to the α variance: $\sigma_\alpha^2 = \sum_m D_\alpha$.

Similarly, the value of the MRD cospectrum ($D_{\beta\alpha}$) between two signals α and β at scale $m+1$ is given by

$$D_{\beta\alpha}(m+1) = \frac{1}{2^M}\sum_{k=1}^{2^M}\overline{\alpha}(k,m)\,\overline{\beta}(k,m), \tag{14}$$

where the sum of $D_{\beta\alpha}$ on all scales is equal to the flux: $\langle\beta'\alpha'\rangle = \sum_m D_{\beta\alpha}$.

One interesting feature of MRD cospectra is the possibility to decompose the flux $D_{\beta\alpha}(m+1)$ at scale $m+1$ between the positive and negative fluctuating quantities $\overline{\alpha}(k,m)\,\overline{\beta}(k,m)$ contributing to the flux at this scale. The positive contribution to the flux at scale $m+1$ is calculated as

$$D^+_{\beta\alpha}(m+1) = \frac{1}{2^M}\sum_{k=1}^{2^M}\overline{\alpha}(k,m)\,\overline{\beta}(k,m)\,I^+, \tag{15}$$

and the negative contribution as

$$D^-_{\beta\alpha}(m+1) = \frac{1}{2^M}\sum_{k=1}^{2^M}\overline{\alpha}(k,m)\,\overline{\beta}(k,m)\,I^-, \tag{16}$$

where I^+ and I^- define the sign of the flux such as when $\overline{\alpha}(k,m)\,\overline{\beta}(k,m)$ is positive $I^+ = 1$ and $I^- = 0$ and the opposite when $\overline{\alpha}(k,m)\,\overline{\beta}(k,m)$ is negative. Hence, $D_{\beta\alpha}(m+1) = D^+_{\beta\alpha}(m+1) + D^-_{\beta\alpha}(m+1)$.

Similarly, the percentage of event number responsible at scale $m+1$ for positive and negative fluxes are, respectively,

$$ND^+_{\beta\alpha}(m+1) = 100 \times nD^+_{\beta\alpha}(m+1)/2^M, \tag{17}$$

and

$$ND^-_{\beta\alpha}(m+1) = 100 \times nD^-_{\beta\alpha}(m+1)/2^M, \tag{18}$$

where $nD^+_{\beta\alpha}$ and $nD^-_{\beta\alpha}$ are the number of events at scale $m+1$ inducing positive and negative fluxes, respectively ($nD^+_{\beta\alpha} + nD^-_{\beta\alpha} = 2^M$).

4. Results

Before presenting the average turbulent transport behavior of momentum, heat, and dust, from the different methods listed in section 3, we find it important to have a qualitative look at the instantaneous behavior of these variables, as measured during wind events (section 4.1), as well as to verify the distribution of their variance according to the eddy frequency (section 4.2).

As already indicated, our analysis will mainly focus on the two main events, 9 March and 20 April, which represent two different wind directions. Figures from the other events are only presented as supporting information S1 as they confirm the findings from the two main events.

4.1. Instantaneous Behavior

Overall, the instantaneous fluctuations of dust number concentration (including all particle sizes) appear much more intermittent, with shaper peaks, than those of meteorological variables (Figure 4). Here "intermittency" is defined as the non-Gaussian aspect of variable time derivative, that is, increments (e.g., Warhaft, 2000). Fluctuations of meteorological variables appear less intermittent and more symmetrically distributed between their mean tendency, that is, lower skewness and kurtosis. The 15-min time series presented in Figure 4 occurred a few hours after the beginning of the 9 March event, when the wind erosion is well established (orange vertical line in Figure 2). Other periods show similar behavior.

Looking more particularly at specific local events, highlighted in gray in Figure 4, we can identify different behaviors between momentum, heat, and dust transports. Event A corresponds to an *uw*-ejection event (negative fluctuation of u, noted u^-, and positive fluctuation of w, noted w^+), transporting a negative momentum flux. This event is associated with positive fluctuations of heat (θ^+) and dust (d^+). Hence, this *uw*-ejection motion transports simultaneously low momentum, warm air, and high dust concentration. Event B is an *uw*-sweep event (u^+ and w^-) transporting simultaneously high momentum, cool air (θ^-), and

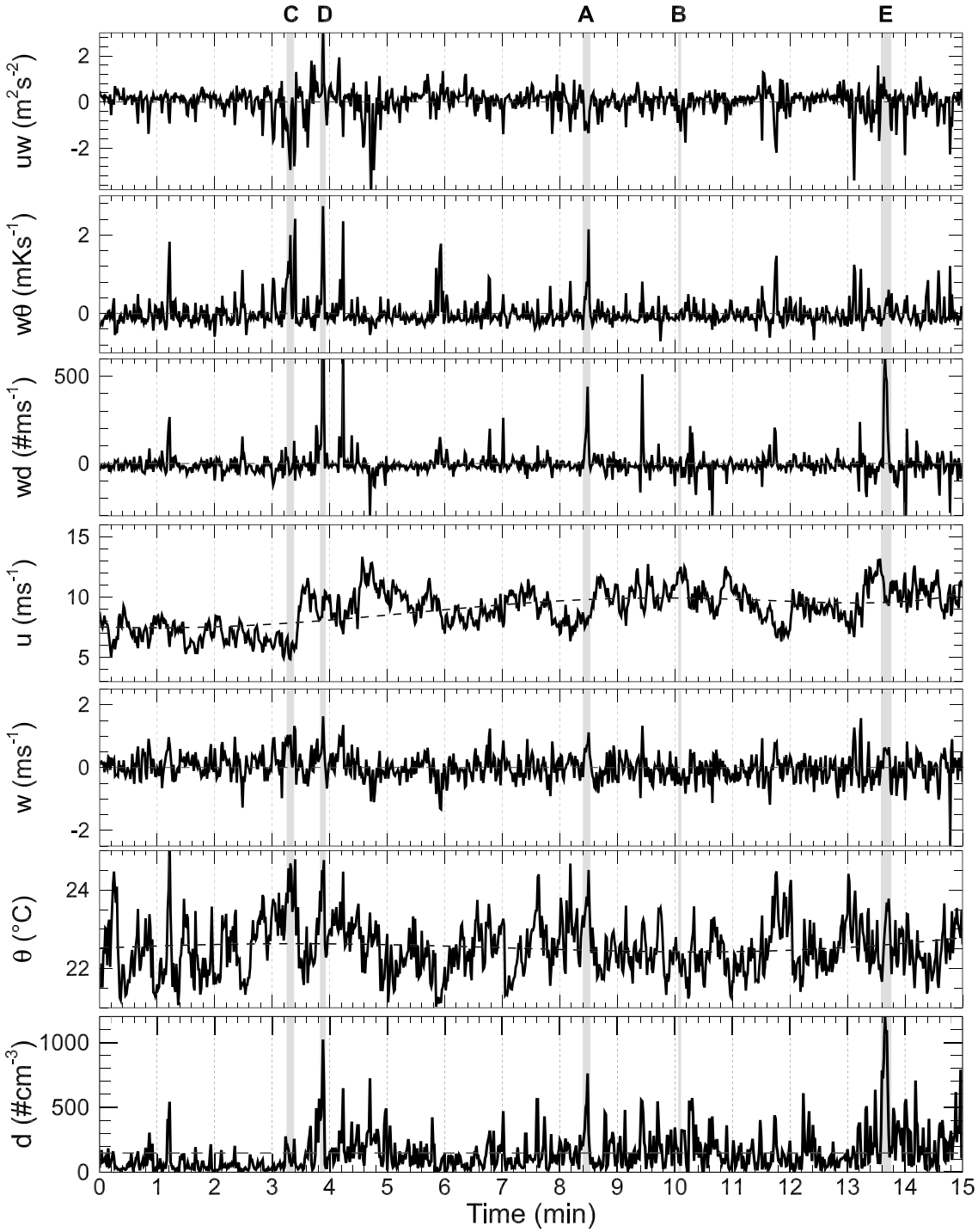

Figure 4. Time series of instantaneous momentum flux (uw), heat flux ($w\theta$), total dust flux (wd), longitudinal wind velocity (u), vertical wind velocity (w), air temperature (θ), and total dust number concentration (d), measured at 3-m height during the first wind event, 2 hr after the beginning of the 9 March wind event (vertical orange line in Figure 2). The horizontal dashed lines represent the average 15-min trend. The letters and gray areas highlight specific events (see the text).

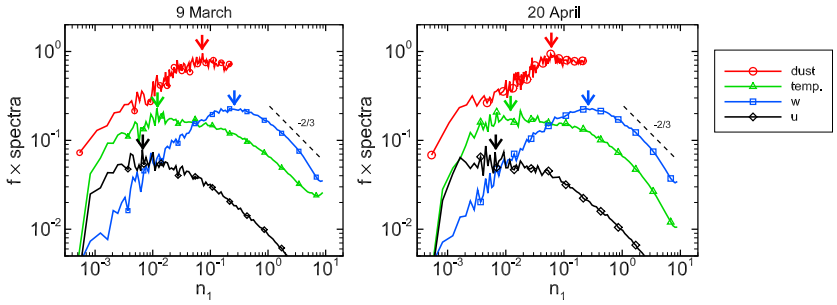

Figure 5. Ensemble-averaged 15-min energy spectra of the longitudinal velocity, vertical velocity, air temperature, and total dust number concentration for the 9 March and 20 April events. The frequency f is normalized by the measurement height z and the mean wind speed at the same height $\langle u \rangle$ such as $n_1 = fz/\langle u \rangle$. Dust and longitudinal velocity spectra are shifted upward and downward, respectively, to permit comparison. The arrows indicate the position of the spectrum peaks. Equivalent figures for the 7 and 8 March and 14 and 16 April events are available in Figure S1.

low dust concentration (d^-). Both events A and B appear in line with a similarity of turbulent transport between momentum, heat, and dust. On the other hand, other events show some dissimilarities. Event C is an uw-ejection event transporting low momentum (u^-) and warm air (θ^+) but no significant dust fluctuations (wd is near zero). For this event, the turbulent transport of dust appears dissimilar with the momentum and heat ones. Events D and E are upward motions (w^+) that transport high momentum (u^+), warm air (θ^+, especially for event D), and high dust concentration (d^+). Here the turbulent transport of momentum appears dissimilar with the heat and dust ones. Although heat and dust fluxes have the same sign during both events, their amplitude compared to the momentum is different between both events.

In conclusion, the similarity between turbulent transport of momentum, heat, and dust is not systematic. One should, therefore, better characterize and understand the dissimilarity between these quantities.

4.2. Energy Spectra

The ensemble-averaged 15-min energy spectra of u and w during both 9 March and 20 April events display the familiar shape of atmospheric surface-layer spectra with a well-defined $-2/3$ power law in the inertial subrange and $+1$ power law in the energy-containing range for the w spectra (Figure 5). The peak positions of the u and w spectra are distant from each other, $n_1 = 0.008$ and 0.32, respectively, where $n_1 = fz/\langle u \rangle$ is the normalized frequency using the measurement height z and the mean wind speed at the same height $\langle u \rangle$. This distance between peak positions is explained by the low roughness of our bare surface, as discussed in Dupont et al. (2018). This reflects the strong anisotropy of the flow near the surface, with large-scale elongated structures corresponding to the low- and high-speed streaks discussed in section 1. The flow becomes isotropic only for frequencies higher than about $n_1 = 1$, when the w spectra reach a $-2/3$ power law.

The air temperature spectra display a much flatter peak, located between the u- and w-spectrum peaks. This flatter peak is consistent with previous observation in near-neutral conditions (e.g., Kaimal et al., 1972), with a peak located here around $n_1 = 0.015$ against 0.030 in Kaimal et al. (1972). For frequencies larger than the w-spectrum peak position, the θ spectra exhibit a slope lower than $-2/3$, meaning that large-scale fluctuations may still contribute to temperature fluctuations at high frequencies (e.g., Warhaft, 2000).

As other variables, the dust spectra exhibit a well-defined energy-containing range with a near $+1$ power law. The dust-spectrum peak at an intermediate position between θ and w spectra, near $n_1 = 0.07$ and 0.06 for the 9 March and 20 April events, respectively. Compared to heat and momentum, the higher frequency position of the dust-spectrum peak could reflect the more local emission of dust with lower mesoscale dust concentration fluctuations. Importantly, after reaching their peak, the dust spectra decrease with the same slope as the temperature spectra up to the cutoff frequency of the dust sensor (1 Hz). This demonstrates the suitability of our dust sensor in measuring dust fluctuations up to 1 Hz.

This behavior of meteorological and dust spectra was observed for all events (Figure S1), except for the 14 April event. For this last event, the dust spectrum appears noisier at high frequency due to the low dust number concentration of this event.

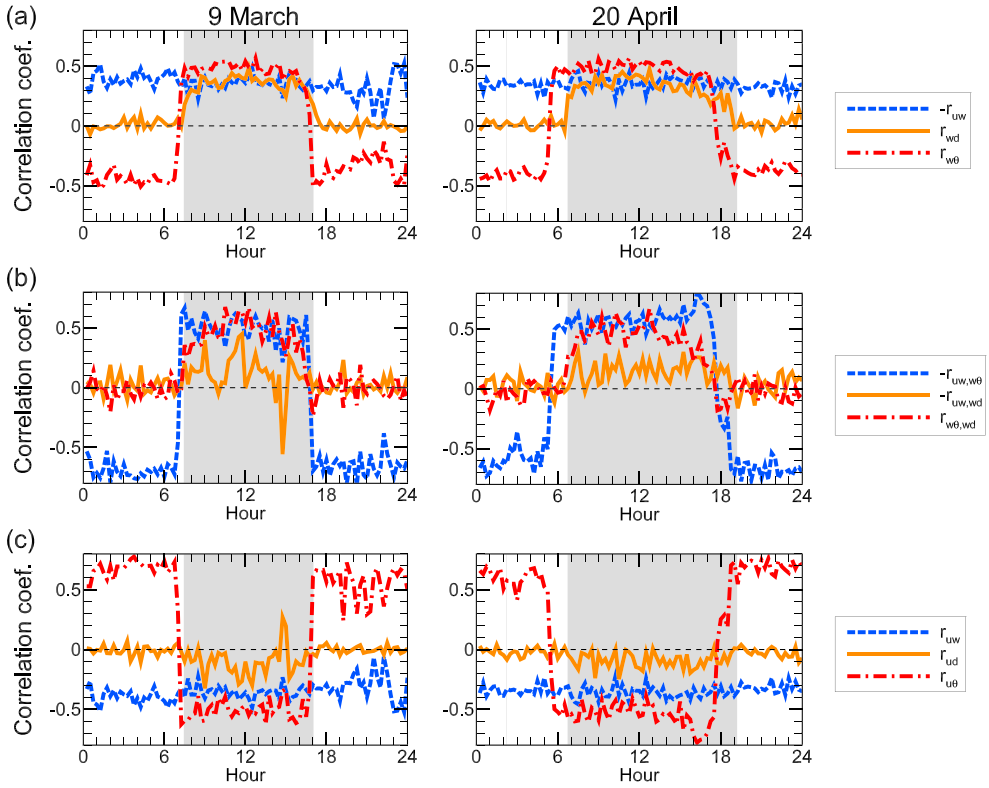

Figure 6. Time variation of the correlation coefficients (a) between the vertical wind velocity and the longitudinal wind velocity, the air temperature, and the concentration of 2.5-μm diameter dust particles ($-r_{uw}$, $r_{w\theta}$, and r_{wd}), (b) between momentum, heat, and 2.5-μm dust fluxes ($-r_{uw,w\theta}$, $r_{w\theta,wd}$, and $-r_{uw,wd}$), and (c) between the longitudinal wind velocity and the vertical wind velocity, the air temperature, and the concentration of 2.5-μm diameter dust particles (r_{uw}, $r_{u\theta}$, and r_{ud}), for the 9 March and 20 April events. Dashed areas indicate periods of wind erosion. Equivalent figures for the 7 and 8 March and 14 and 16 April events are available in Figure S2.

4.3. Correlation Coefficients

During both 9 March and 20 April events, the correlation coefficients for the momentum and heat fluxes, r_{uw} and $r_{w\theta}$, respectively, reach on average usual values observed in the surface boundary layer (e.g., Kaimal & Finnigan, 1994), about −0.35 for r_{uw} and +0.50 and −0.40 for $r_{w\theta}$ during daytime and nighttime, respectively (Figure 6a). The difference between r_{uw} and $r_{w\theta}$ shows that heat is more efficiently transported by the w fluctuations than the momentum. Note that $r_{w\theta}$ changes sign as a consequence of the diurnal cycle. Interestingly, both correlation coefficients appear unaffected by the presence of soil erosion (dashed areas in Figure 6a). The correlation coefficient r_{wd} for 2.50-μm particles (bin 4) is close to $-r_{uw}$ during both erosion events. As expected, without erosion, r_{wd} is close to zero.

The momentum and heat fluxes appear well correlated, $r_{uw,w\theta} \approx -0.50$ during daytime, with a slightly higher correlation on the 20 April event, probably related to a small difference in atmospheric stability (Figure 6b). The heat and 2.50-μm dust fluxes are also relatively well correlated during the erosion events; $r_{w\theta,wd}$ is close to $-r_{uw,w\theta}$. However, $r_{uw,wd}$ is low, around −0.2 with large fluctuations, while separately, heat and dust fluxes, and heat and momentum fluxes, are correlated. This may suggest that the correlation between heat and dust does not have the same distribution in frequency as the correlation between heat and momentum. Figure 6c shows that the low value of $r_{uw,wd}$ is due to the poor correlation between d and u fluctuations compared to that between θ and u and between w and u fluctuations ($r_{ud} \approx -0.1$, $r_{uw} \approx -0.4$, $r_{u\theta} \approx -0.6$). In conclusion, when integrating over all eddy sizes, a larger dissimilarity exists in the turbulent transport between momentum and dust than between heat and dust.

In other erosion events (supporting information S1), the correlation coefficients exhibit similar behaviors. The coefficient r_{uw} is slightly lower at midday on 7 March and 14 April due to the more convective conditions (see Figure S2). Interestingly, the dust concentration and streamwise velocity fluctuations correlate

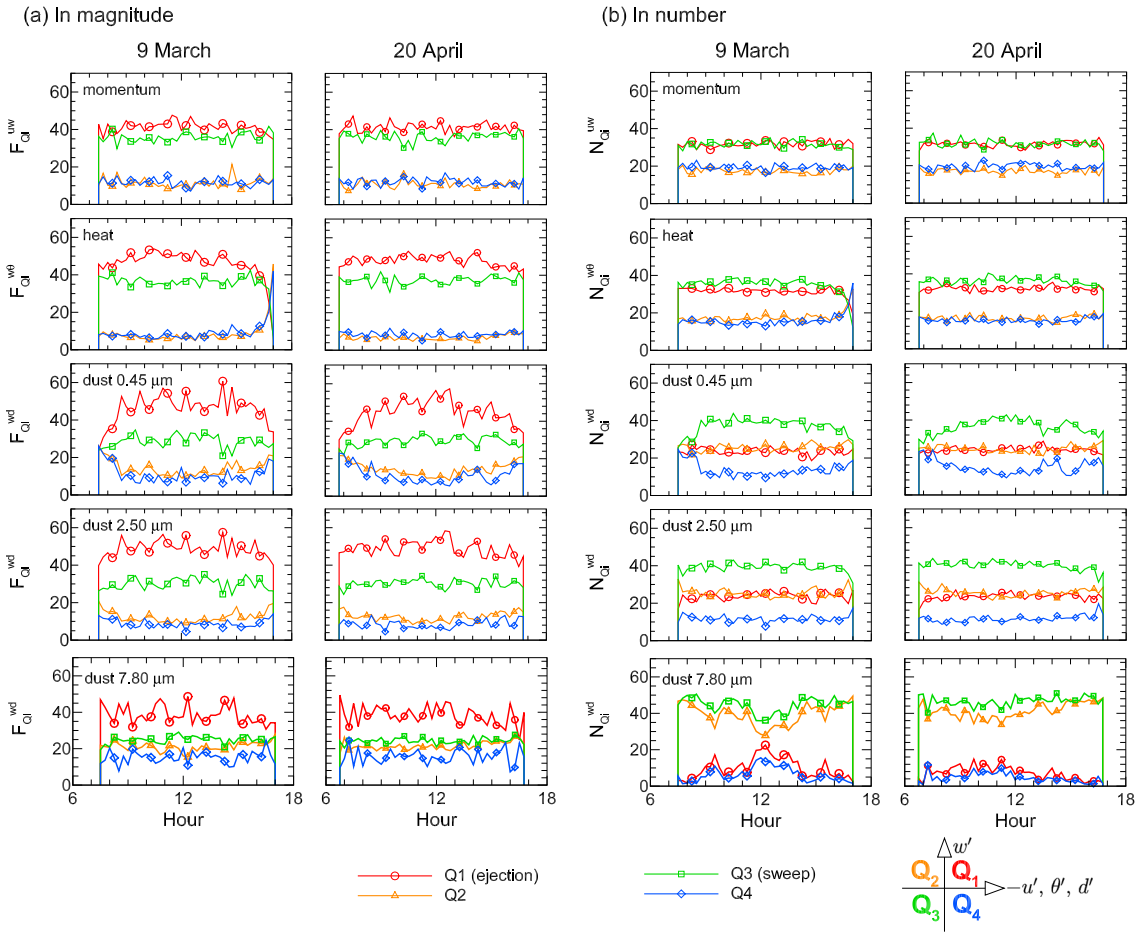

Figure 7. Time variation of the fractions in magnitude (a) and in event number (b), of the momentum ($\langle u'w' \rangle$), heat ($\langle w'\theta' \rangle$), and size-resolved dust ($\langle w'd' \rangle$) fluxes in each quadrant as defined in equations (2) and (3), respectively, for the 9 March and 20 April events. For clarity purpose, values outside wind erosion periods are not presented. Equivalent figures for the 7 and 8 March and 14 and 16 April events are available in Figure S3.

better around 1 pm and from 10 am to 2 pm during the 8 March and 16 April events, respectively ($r_{ud} \approx 0.4$, Figure S2), leading to higher values of $r_{uw,wd}$ (≈ -0.4). These two periods were characterized by high wind speed, suggesting that the wind intensity may impact r_{ud} and $r_{uw,wd}$. Regarding the sensitivity of the correlation coefficients to the particle size (result not shown), similar correlation coefficients were observed for all particle diameters lower than 7.80 μm (bins 1 to 5). For larger particles (bins 6 and 7), the correlation coefficients decrease as particles become less numerous. The volume of the sampling air collected by the particle spectrometer is probably too low to reach a meaningful dust concentration for such large and rare particles. This was visible from the step-function aspect of the concentration signal for large particles, that is, a signal with visible incremental variations of low dust particle number.

4.4. Quadrant Analysis

The percentages of the vertical momentum $\langle u'w' \rangle$, heat $\langle w'\theta' \rangle$, and dust $\langle w'd' \rangle$ fluxes, in each quadrant, are presented in number of events and in magnitude of the flux, as defined in equations (2) and (3), in Figures 7a and 7b, respectively, during the 9 March and 20 April events. For clarity, values outside the erosion events are not presented. The mean values obtained for each event are summarized in Table 1. This quadrant partition of the dust flux is presented in Figure 7 for three particle sizes, 0.45, 2.50, and 7.80 μm, corresponding to bins 1, 4, and 6 in Figure 3a and for all particle bins in Table 1.

In agreement with current understanding (e.g., Robinson, 1991), the turbulent transport of momentum and heat in near-neutral surface boundary layer occurs mainly via sweeps (Q3) and ejections (Q1), with a slight domination of ejections in magnitude and domination of sweeps in number, especially for heat. Ejections and sweeps transport on average about 41% and 36% (32% and 32%) of the momentum flux in magnitude (in

number), respectively, and 47% and 36% (31% and 35%) of the heat flux. This partition in quadrants exhibits low variability during and between erosion events (Figures 7a and 7b), except for the inversion of the heat flux partition due to the diurnal cycle. This partition in quadrants of the momentum and heat fluxes confirms a relative close similarity in turbulent transport between momentum and heat in near-neutral conditions.

The partition of the dust flux between the four quadrants is slightly different. As momentum and heat, dust appears mainly transported by ejections (Q1) and sweeps (Q3) for particles smaller than 7.80 μm (first five bins), with small partition differences according to the particle size (Table 1). In magnitude, the Q1 contribution dominates with a similar proportion as for the heat flux (near 49%). The Q3 contribution appears lower than for momentum and heat fluxes, near 30% against 36%, respectively, although it is still higher than the contributions from Q2 and Q4. In number, this is the opposite; Q3 dominates with a larger proportion than for momentum and heat fluxes, 39% against 32% and 35%, respectively, and Q1 has a lower contribution than for momentum and heat, near 24% against 32% and 32%, respectively. The most striking feature is the higher contribution of Q2 in number in the dust flux than in the momentum and heat fluxes, about 25% against 17%, respectively. Hence, the Q2 contribution in number is slightly higher than the Q1 contribution in transporting dust particles. In magnitude, Q1 remains larger than Q2 as for heat and momentum fluxes. This dust partition is observed for all events (see Figure S3).

Interestingly, in magnitude, the Q1 contribution seems to increase with wind intensity for 0.45-μm particles (less for particles >0.45 and ≤7.80 μm), while Q2 and Q4 contributions decrease, and Q3 contribution remains stable (Figure 7a). This dependence to the wind intensity is especially visible on the 7 and 8 March and 16 April events whose mean wind speeds vary significantly during the event (Figure S3). This is less visible in number.

For larger particles (>7.80 μm, the last two bins), the contribution in number of quadrants with negative dust fluctuations (Q2 and Q3) increases, to represent almost 50% of the events for particles larger than 10 μm (Table 1). This results from the scarcity of large particles in the air.

4.5. Octant Analysis

To identify whether momentum quadrant events transport positive or negative heat (θ) and dust (d) fluctuations, Figures 8a and 8b present the octant analysis of the momentum flux following the sign of the temperature and dust fluctuations for both main erosion events. As for the quadrant analysis, dust fluctuations are presented for three particle bins, 0.45, 2.50, and 7.80 μm.

As expected, uw-ejection (Q1) and uw-sweep (Q3) motions correlate well with θ^+ and θ^-, respectively. This result is verified for all wind events (see also Figure S4) and for the quadrant partition of the momentum flux in both magnitude and number of events. Although the atmospheric stability is near-neutral, the correlation of the momentum flux with the temperature fluctuations is not zero because the erosion events occurred mostly in the unstable side of the near-neutral conditions. Hence, heat is closely transported as momentum.

Conversely to temperature fluctuations, uw ejections (Q1) appear weakly correlated in magnitude with positive dust fluctuations of small particles (< 7.80 μm), Q1 (d^+) being slightly larger than Q1 (d^-) in Figure 8. In number, uw ejections are mostly uncorrelated with fluctuations of small dust particles, meaning that the dust emission does not occur preferentially during uw ejections. However, uw ejections and uw sweeps correlate better with d^+ and d^-, respectively, with increasing wind speed. This is especially visible in magnitude partition for 2.50-μm particles during the 7 and 8 March and 16 April events (Figure S4). It is worth noting that uw-Q4 motions (u^- and w^-) appear better correlated with d^- than with d^+, which was not observed for temperature fluctuations.

Overall, uw ejections clearly do not transport heat and small dust particles similarly when including all ejection frequency range. These results are confirmed by other events (see Figure S4). For particles larger than 7.80 μm, uw ejection and uw sweep become more correlated with d^- due to the scarcity of large particles.

4.6. Fourier Cospectra

To identify the time frequency of the main turbulent structures contributing to the vertical momentum, heat, and dust fluxes, Figure 9a compares the ensemble-averaged 15-min $-uw$, $w\theta$, and wd cospectra ($-S_{uw}$, $S_{w\theta}$, and S_{wd}) obtained at 3-m height, for both erosion events. The cospectra have been normalized by their maximum values in order to compare their distribution. We only present dust flux cospectra for 2.50-μm-diameter particles as other particle sizes give similar behavior. Although large particles (≥7.80 μm) were rare and

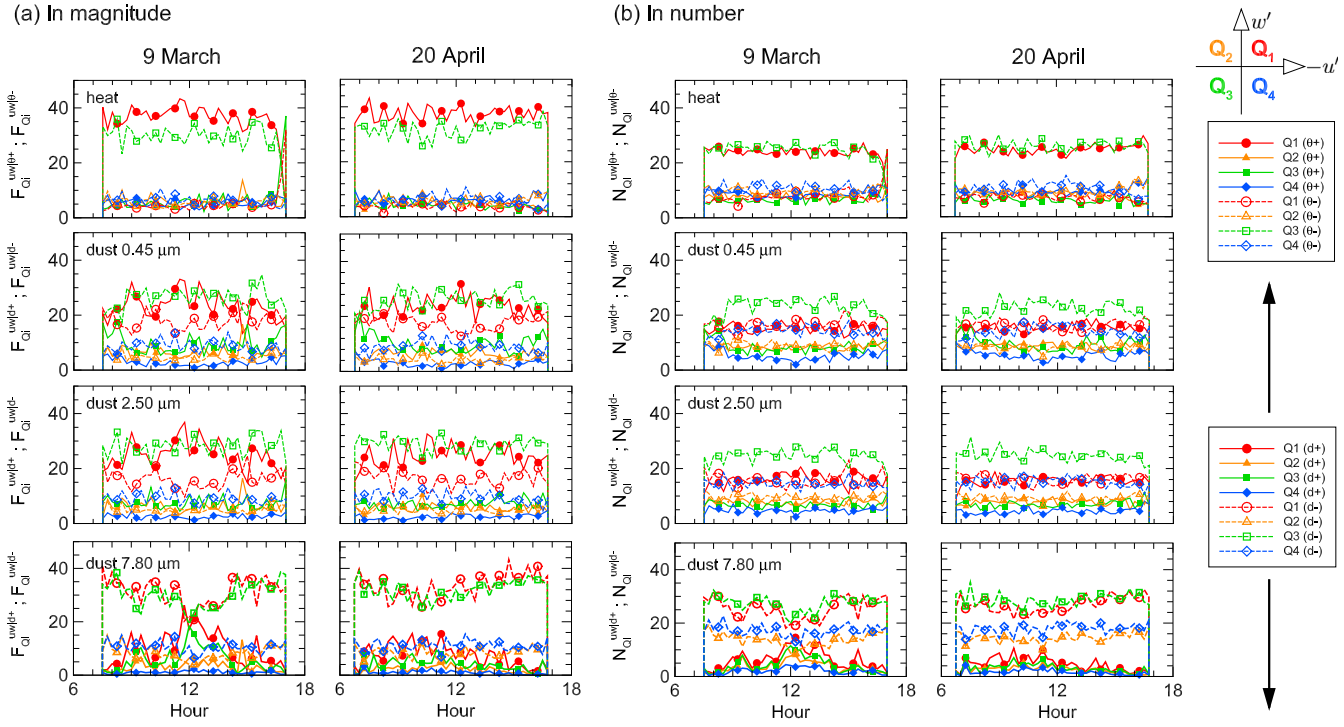

Figure 8. Time variation of the fractions in magnitude (a) and in event number (b), of the momentum flux ($\langle u'w' \rangle$) in each quadrant and associated with positive or negative temperature (θ^+, θ^-) and size-resolved dust concentration (d^+, d^-) fluctuations, as defined in equations (6)–(9), for the 9 March and 20 April events. For clarity purpose, values outside wind erosion periods are not presented. Equivalent figures for the 7 and 8 March and 14 and 16 April events are available in Figure S4.

probably undersampled by the particle spectrometer, the cospectra of their flux have a similar distribution with frequency as smaller particles, with more perturbations (result not shown).

The $-uw$ and $w\theta$ cospectra display an expected shape with a well-defined $-4/3$ power law in the inertial subrange and +1 power law in the energy-containing range (power laws not shown in Figure 9 as the figure is in semilog coordinates). Both cospectra superpose in the energy-containing range, that is, low-frequency side of the peak. As observed by Kaimal et al. (1972), the peak of the $w\theta$ cospectra is flatter than the uw-cospectrum peak, shifting the inertial subrange of the $w\theta$ cospectra to higher frequencies. This shift means that smaller eddies transport more efficiently heat than momentum. The peak locations of the uw and $w\theta$ cospectra are close to the values reported in Kaimal et al. (1972), around $n_1 = 0.03$ and 0.05–0.10 here, against $n_1 = 0.07$ and 0.10 in Kaimal et al., 1972, respectively.

Despite the low frequency of our particle spectrometer (1 Hz), most of the dust flux was captured (more than 80%), only the high-frequency part was missing (Figure 9a). The wd cospectra exhibit a peak close to the uw-cospectrum ones, around $n_1 = 0.03$, for both events. In the energy-containing range, the wd cospectra have less energy with a steeper slope than the uw and $w\theta$ cospectra. This means that dust is not vertically transported or emitted by large-scale motions as well as momentum and heat. Passing the cospectrum peak, the wd cospectra decrease on the high-frequency side similarly as the uw cospectra, with a slightly steeper slope in the inertial subrange. Since the decrease of the d spectrum at this frequency range ($0.07 \leq n_1 \leq 0.20$) was consistent with the θ-spectrum one (Figure 5), this steeper slope of the wd cospectra is expected to be true and not related to a loss of correlation of the dust sensor with the flow. The time lag between w and d was also too small to lead to a loss of correlation (see section 2.3). This behavior of wd cospectra is supported by other events (see Figure S5a).

At low frequencies, heat and dust appear horizontally transported differently (Figure 9b). While the $u\theta$ cospectra exhibit a similar shape as the one observed in Kaimal et al. (1972), with one main peak near $n_1 = 0.01$, the ud cospectra exhibit surprisingly two peaks, a positive one at low frequency, near $n_1 = 0.002$, and a negative one at midfrequency range, near $n_1 = 0.03$, close to the uw-cospectrum peak. This behavior is confirmed by other erosion events (see Figure S5b), although the positive peak at low frequency appears

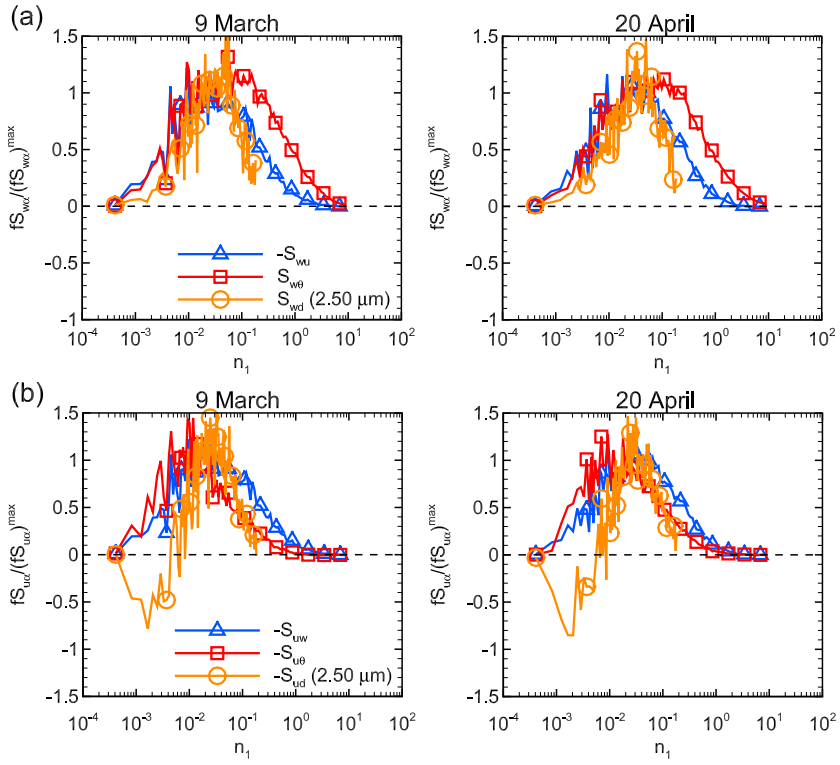

Figure 9. Comparison of the ensemble-averaged 15-min normalized Fourier cospectra of the vertical (a) and horizontal (b) momentum, heat, and 2.5-μm dust fluxes, at 3-m height, for the 9 March (left figures) and 20 April (right figures) events. Cospectra are normalized by their maximum. The frequency f is normalized by the measurement height z and the mean wind speed at the same height $\langle u \rangle$ such as $n_1 = fz/\langle u \rangle$. Equivalent figures for the 7 and 8 March and 14 and 16 April events are available in Figure S5.

weaker for the 8 March and 16 April events. The negative peaks of the $u\theta$ and ud cospectra, around $n_1 = 0.01$ and 0.03, respectively, result from both the maximum of the vertical heat and dust fluxes (emission) and the large negative correlation between w and u, at these frequencies (Figure 9a). Hence, heat and dust emissions are mainly explained by uw-ejection and uw-sweep motions at these frequencies. The difference between $u\theta$ and ud cospectra at low frequencies suggests a different emission or horizontal transport between heat and dust at these frequencies. This is discussed in section 5.

4.7. MRD Cospectra

The MRD cospectra of the vertical and horizontal momentum, heat, and dust fluxes exhibit the same shape as the Fourier cospectra for all events (Figures 10 and S6). The main difference lays on the peak locations, which are slightly shifted toward higher time scales in the MRD cospectra. This shift is explained by the difference of definition of turbulent structures between MRD and Fourier methods. Turbulent structures are defined in time scale in MRD and in frequency of passage in Fourier method. Hence, the MRD-cospectrum peaks correspond to the time scales of the main eddies contributing to the flux, while the Fourier-cospectrum peaks correspond to the frequencies of these main eddies. The similarity in cospectrum shape between both methods gives us confidence in the significance of the differences observed in the previous section between Fourier cospectra of heat, momentum, and dust fluxes.

The MRD method allows to look at the partition of the MRD cospectra between the positive and negative component of the fluxes, referred hereafter by the exponents $^+$ and $^-$, respectively. The distribution in magnitude between scales of the positive and negative (negative and positive) components of the vertical heat (momentum) and dust fluxes appears similar in both erosion events (Figure 11a). Here the MRD cospectra have been normalized by the maximum of their positive component (negative component for the momentum flux) to facilitate their comparison. Only a lower contribution of the large scales to wd^+ is visible compared to $w\theta^+$ and uw^-. This explains the lower contribution of low frequency motions to the dust flux observed from the wd cospectra compared to the uw and $w\theta$ cospectra (Fourier cospectra in Figure 9a and

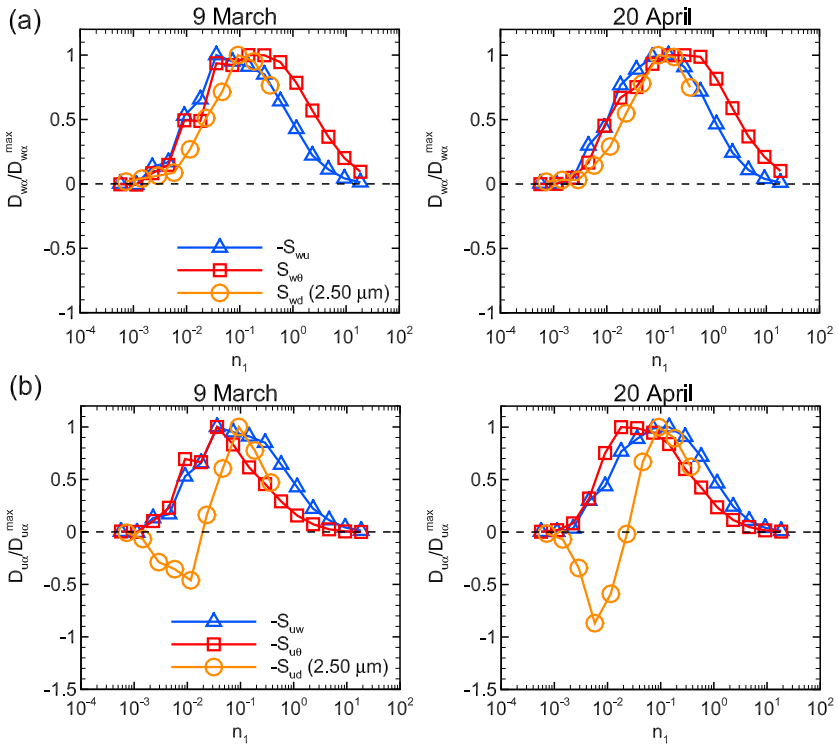

Figure 10. Same as Figure 9 but for the multiresolution decomposition cospectra. On the abscissa, the inverse time scale is normalized by the measurement height z and the mean wind speed at the same height $\langle u \rangle$ such as $n_1 = z/(timescale \times \langle u \rangle)$. Equivalent figures for the 7 and 8 March and 14 and 16 April events are available in Figure S6.

MRD cospectra in Figure 10a). The uw^+ and $w\theta^-$ cospectra have similar shape, while the wd^- cospectrum slightly increases at inverse time scales higher than $n_1 = 0.1$. This explains the subtle faster decrease in the inertial subrange of the wd cospectrum compared to uw and $w\theta$ cospectra (Fourier cospectra in Figure 9a and MRD cospectra in Figure 10a).

The partition of the MRD cospectra of horizontal fluxes between their positive and negative components shows differences between heat and dust fluxes (partition in magnitude in Figure 11b and in number in Figure 12b) for both erosion events. Here the cospectra have been normalized by the maximum of the negative component of the cospectra (positive component for the momentum flux). On one side, the $u\theta^+$ and ud^+ cospectra exhibit the same distribution with inverse time scale, with the same peak location around $n_1 = 0.01$, while uw^+ peaks at higher inverse time scales, around $n_1 = 0.4$. On the other side, the ud^- cospectra appear much lower in amplitude than the $u\theta^-$ cospectra, with a peak shifted toward higher inverse time scales (Figure 11b). This lower amplitude of ud^- cospectra is related to the largest number of eddies carrying negative correlations between u and d fluctuations, especially at small inverse time scales (Figure 12b). This difference explains the positive horizontal dust flux at low frequency observed in Fourier and MRD cospectra (Figures 9b and 10b) and the shifted maximum toward high frequencies of the Fourier and MRD ud cospectra compared to the $u\theta$ cospectra.

As for Fourier cospectra, other erosion events confirm this partition of MRD cospectra between positive and negative components of the fluxes (see Figures S7 and S8). This partition is also not significantly affected by the size of the particles (result not shown).

5. Discussion

The main goal of the present study was to verify the hypothesis of similarity between dust, heat, and momentum transport during aeolian soil erosion, a hypothesis usually considered when assessing the particle flux from an indirect approach such as the flux-gradient, flux-variance, or relaxed eddy accumulation methods.

As expected, the dissimilarity between momentum and heat transport remained limited during erosion events as the atmospheric stability was near-neutral. The heat flux was too low to produce significant buoy-

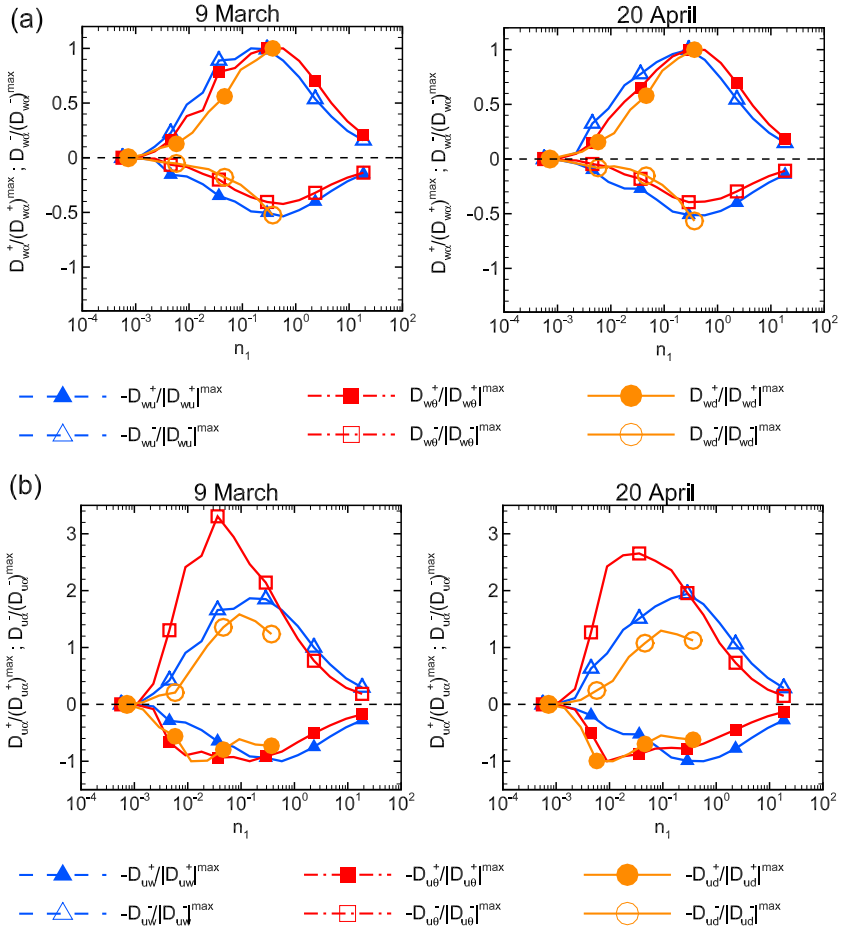

Figure 11. Same as Figure 10 but the multiresolution decomposition cospectra have been partitioned in magnitude between the positive and negative components of the fluxes (equations (15) and (16)). The cospectra of vertical (horizontal) fluxes have been normalized by the maximum of the positive (negative) component of the cospectra. Equivalent figures for the 7 and 8 March and 14 and 16 April events are available in Figure S7.

antly driven turbulence. As previously observed in surface boundary layer (e.g., Kaimal et al., 1972), the main difference between turbulent transport of heat and momentum was the higher efficiency of turbulence, especially small eddies, at transporting heat than momentum. This was visible from (1) the larger correlation coefficient $r_{w\theta}$ than r_{uw} (Figure 6), (2) the higher proportion of $w\theta$ ejections at transporting heat than uw ejections at transporting momentum (Table 1), and (3) the larger contribution of the $w\theta$ cospectra at high frequency (Figure 9a). This weak dissimilarity between heat and momentum results from the occurrence of soil erosion during daytime, leading to stability conditions preferentially located on the unstable side of the near-neutral conditions.

Our measurements revealed a different partition of the dust and momentum-heat fluxes following the type and time scale of turbulent structures. In particular, the partition of the vertical fluxes in quadrants showed a much lower number of events contributing to the vertical transport of positive dust fluctuations (w^+d^+) than to the vertical transport of positive heat ($w^+\theta^+$) and negative momentum (w^+u^-) fluctuations, while the vertical transport of negative dust fluctuations (w^+d^-) was higher (Table 1). The distribution of the fluxes according to the eddy frequencies (Fourier cospectra) and the eddy time scales (MRD cospectra) further showed a difference in transport between dust and momentum-heat. Dust was not transported vertically by the low-frequency motions as well as heat and momentum, the dust flux cospectra increasing slower with increasing frequency in the energy-containing range (Figure 9a). Unlike heat and momentum, dust fluctuations correlated also differently with u fluctuations between low- and high-frequency motions. At low frequency ($n_1 < 0.006$), u correlated positively with d, while it correlated negatively with θ and w fluctuations (Figures 9b and S5b). This opposite correlation of d and u between low and high frequencies

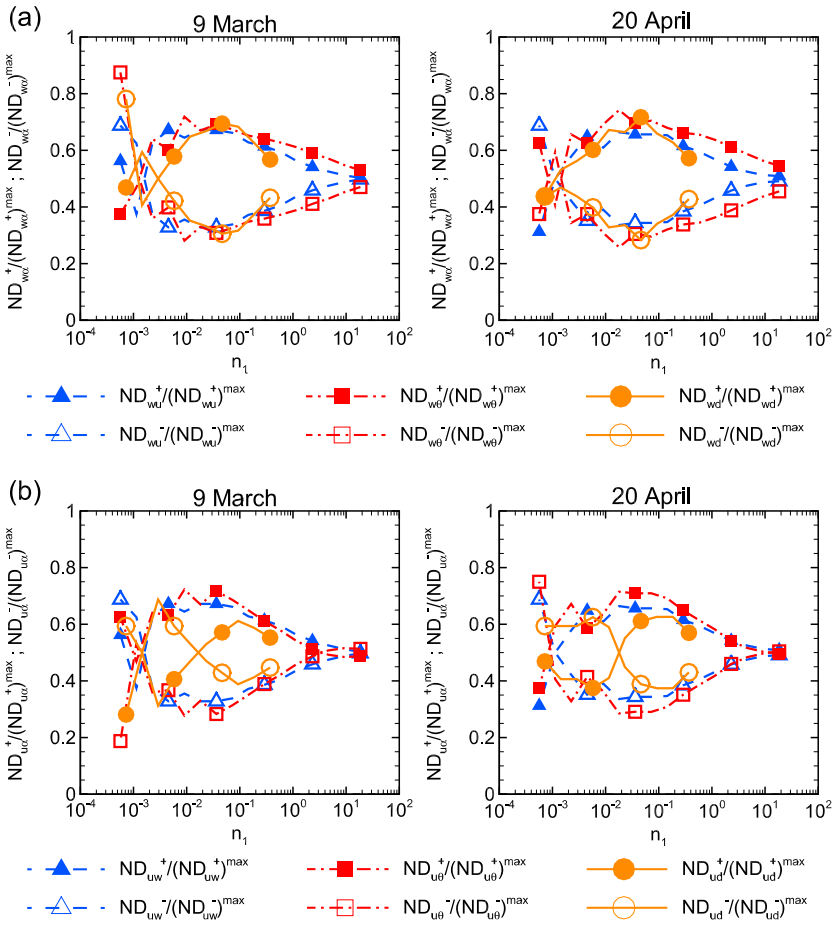

Figure 12. Same as Figure 11 but the partition has been done in number instead of in magnitude (equations (17) and (18)). Equivalent figures for the 7 and 8 March and 14 and 16 April events are available in Figure S8.

led to a poor correlation between the vertical dust and momentum fluxes when integrating over all eddy sizes (Figure 6). At small scales, dust appeared closely transported as momentum, although for some events, the *wd* cospectra decrease slightly faster with frequency than the *uw* cospectra. This last feature is more pronounced on the Fourier cospectra than on the MRD ones (see Figures 9a and 10a). As momentum, dust is, thus, less efficiently vertically transported than heat by small eddies. However, measurements with an higher frequency dust sensor would be necessary to confirm this result at small scales.

The dissimilarity between dust and momentum-heat fluxes was observed for all particle sizes between 0.3 and 5.6 μm (first five bins) as well as for all erosion events, with roughly the same level of dissimilarity. Above 7.8 μm (last two bins), the number of detected dust particles was too low to reach meaningful correlations with wind velocity fluctuations although *wd* cospectra exhibit the same pattern as for smaller particles. This last behavior suggests that the same mechanism of turbulent transport still occurs for larger particles, at least up to 20 μm. Above this size, particle inertia and gravity are known to become significant.

This dissimilarity is most likely related to differences in the surface sources/sinks between dust and momentum-heat. Indeed, at 3-m height, the turbulence transporting momentum, heat, and mass are dominated by anisotropic attached eddies, that is, eddies in contact with the surface (Townsend, 1976). Eddies become isotropic only for $n_1 > 1$ following the location of the inertial range of the *w*-Fourier spectrum (Figure 5). Conversely to heat emission and momentum absorption, dust emission is conditioned by a threshold surface wind shear above which occur successively saltation and dust emission through sandblasting. This mechanism may lead to a more intermittent dust emission compared to the more continuous heat emission and momentum absorption, especially at large scales ($n_1 < 0.006$). Hence, all eddies in contact with the surface do not lead simultaneously to emission of heat and dust and to absorption of momentum,

and thus do not transport similarly dust and momentum-heat. The impact of the dust emission intermittency on the dust turbulent transport at 3 m high is probably accentuated here by the dominant local origin of dust particles from our isolated plot.

The intermittency of soil erosion is well known and visible from the blowing sand structures near the surface, known as aeolian streamers (e.g., Baas & Sherman, 2005; Dupont et al., 2013), surrounded by regions of lower or no saltation (no dust emission) according to the wind intensity. The presence of aeolian streamers surrounded by regions without saltation was clearly observed on the field during erosion events. This intermittency was visible in our measurements from (1) the instantaneous time series of dust concentration compared to temperature and horizontal wind velocity time series (Figure 4), (2) the larger number of ejections transporting low momentum (w^+u^-), warm air ($w^+\theta^+$), and "clean air" (w^+d^-) instead of "dusty air" (w^+d^+), as shown by the quadrant analysis (Table 1), and (3) the positive correlation of u^+ and d^+ at large scales (Figures 9b and 10b). Interestingly, Porch and Gillette (1977) also observed a larger intermittency for dust concentration than for horizontal wind speed time series but to a lesser extent than here. Our MRD partition analysis further showed that the lower efficiency of large-scale motions at transporting dust vertically is related to a lower contribution of the positive component of the flux (Figure 11a), itself probably due to the scarcer emission of dust.

The spatial heterogeneity of the saltation process and, thus, of the dust emission is more likely related to the flow turbulence rather than to the heterogeneity of the surface (Dupont et al., 2013). As reviewed in section 1, the main turbulent structures present at large scales in the near-surface atmospheric layer are juxtaposed meandering regions of low- and high-speed streaks, often referred to as Very Large Scale Motions. These large-scales structures with time scales of about few minutes are responsible for most of the saltation flux variability (see, e.g., the Figure 7 of Liu et al., 2018). We suspect that for our wind conditions, the saltation occurred essentially during high-speed streaks, as the threshold velocity for particles to enter into saltation should have been more often exceeded during such structures. This would explain the positive correlation between u^+ and d^+ observed at large scales (a few minutes time scale as well). Positive fluctuations of temperature (θ^+) do not correlate with u^+ at large scales because of the more continuous emission of heat over the eddy size range of the flow and the absence of a threshold mechanism linked to the wind intensity for releasing heat. This active role of strong large-scale motions to release dust, and not only transporting dust as for momentum and heat, was first mentioned by Gillette and Porch (1978) who also observed from a field experiment that a large portion of the dust flux was correlated to the strongest horizontal wind speeds. More recently, Wang et al. (2017) also observed a positive correlation between u and mineral dust concentration (PM_{10}) for time scales of several minutes. They also attributed this correlation to the link between dust emission and the passage of high-speed Very Large Scale Motions. At high frequency ($n_1 > 0.006$), ejection motions (w^+ and u^-) are the most energetic gusts transporting-releasing dust (d^+) and heat (θ^+; Figure 9a). Hence, positive fluctuations of dust and temperature become correlated with u^-. These ejection motions are expected to be embedded within the larger-scale streaks. The passage of large-scale elongated structures with intense wind, during several minutes, producing saltation, with local gusts releasing dust in the atmosphere, was inferred on the field from the observation of elongated high dust concentration plumes.

With increasing friction velocity, the dissimilarity between dust and momentum-heat turbulent transports diminishes for small particles ($\leq$2.5 μm). This is inferred from (1) the enhancement of the percentage of w^+d^+ in magnitude of the dust flux and, to a lesser extent, in event number, with the friction velocity, reaching values close to those for the heat flux (Figures 13a and 7 for the dust and heat flux quadrants, respectively), (2) the increase of the proportion of uw ejection carrying d^+ with the friction velocity (Figure 13b), and (3) the increase of the correlation coefficient between momentum and dust fluxes with the friction velocity (Figure 14). We suspect that with increasing wind speed, aeolian streamers become more spatially continuous and thus dust emission. According to the saltation transport patterns identified by Baas and Sherman (2005) following the wind conditions, aeolian streamers become embedded in larger saltation structures in higher wind conditions. Hence, under high wind conditions, saltation and dust emission are no longer restrained to the passage of large-scale high-speed streaks but become more homogeneous in space and in frequency as are heat and momentum. This explains the lower positive correlation between d and u observed at large scales for the 8 March and 16 April events (Figure S5b), whose wind intensities were slightly larger than for the other events. Our measurements indicate that dust transport becomes closer to the momentum and heat ones for friction velocities above 2.5 to 3.0 times the threshold friction velocity (i.e., u_{*0} around 0.55 and 0.66 ms^{-1}), based on the extrapolation of the $-r_{uw,wd}$ trend with u_{*0} to the value

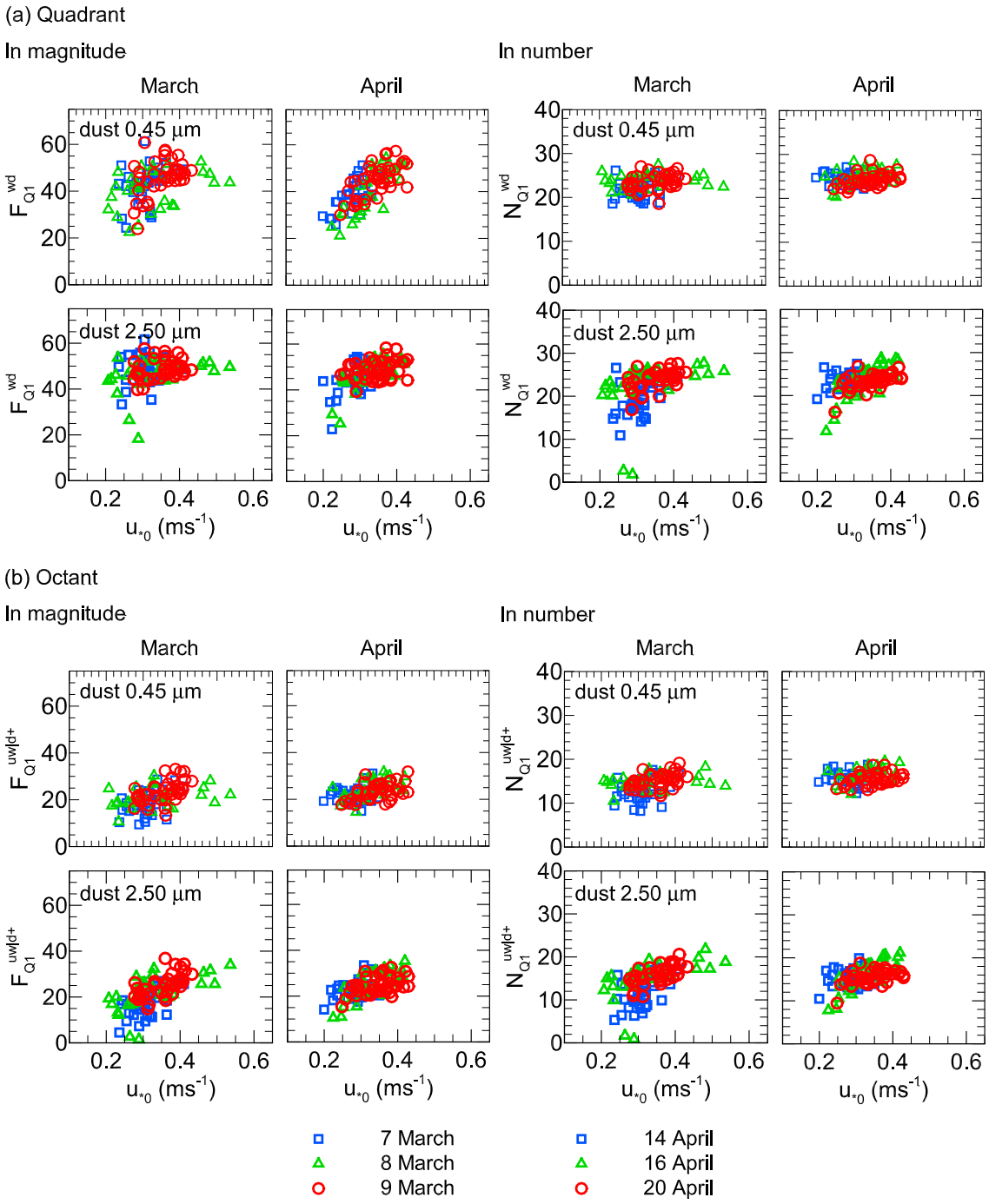

Figure 13. (a) Q1 fraction of the size-resolved dust flux and (b) Q1 fraction of the momentum flux carrying positive fluctuations of dust (d^+), as a function of the surface friction velocity, for all erosion events and for the first two size bins. Both fractions are expressed in magnitude (left) and event number (right) of the fluxes.

of $-r_{uw,w\theta}$ in Figure 14 (dash-dotted line). However, we did not observe any reduction of the intermittent aspect of the dust number concentration time series (i.e., skewness and kurtosis of the concentration time derivative) with increasing friction velocity (result not shown). The strongest periods of the erosion events were probably too short in time for observing such intermittency reduction. Interestingly, this sensitivity to the wind intensity of the similarity between dust and heat turbulent transports may explain the dissimilarity observed by Fratini et al. (2007) between dust and heat flux cospectra for their lowest wind event (friction velocity around 0.40 ms^{-1}) while similarity was observed for their highest event (0.60 ms^{-1}).

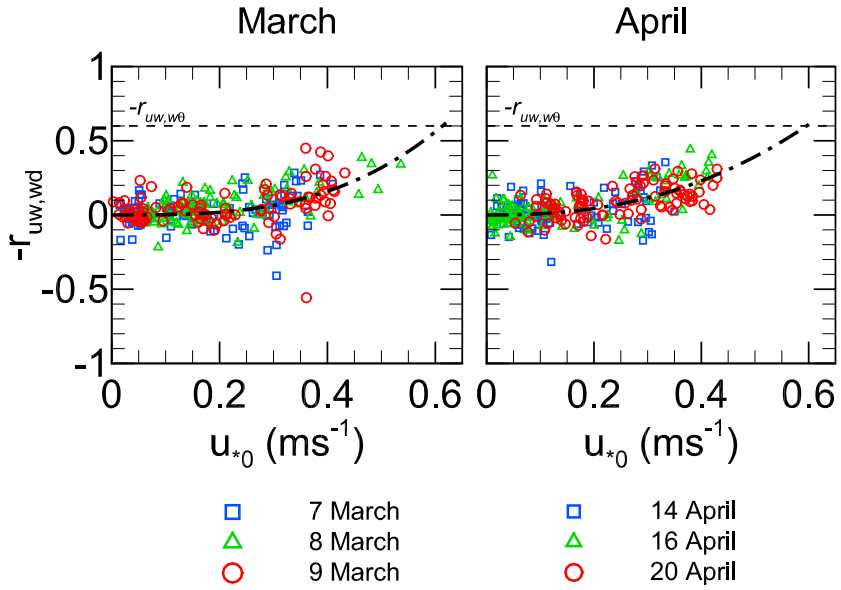

Figure 14. Correlation coefficient between momentum and 2.5-μm dust fluxes ($-r_{uw,wd}$) as a function of the surface friction velocity, for all erosion events. The dashed horizontal lines indicate the mean value of $-r_{uw,w\theta}$ during daytime, and the dash-dotted lines represent a power fit up to the value of $-r_{uw,w\theta}$.

Overall, our results show strong evidence of dissimilarity between the transport of dust, heat, and momentum for wind conditions leading to sparse saltation patterns. For stronger winds, when saltation becomes fully spatially developed, the dust turbulent transport gets closer to the momentum one, although the dust concentration still appears more intermittent than the temperature and wind velocities. The link between the sparseness of dust emission and the dissimilarity between dust and momentum transports suggests that this dissimilarity could be accentuated with decreasing surface erodibility such as in presence of crusting surface. Indeed, the presence of nonerodible roughness elements on the surface may attenuate the spatial development of saltation patterns while impacting less the heat emission and momentum absorption.

This dissimilarity between dust and momentum-heat for wind conditions where saltation is not fully spatially developed, may impact the evaluation of the dust flux from the traditional flux-gradient approach or other approaches assessing dust flux based on the similarity with other scalar quantities, such as the flux variance (e.g., Katul et al., 1995) or relaxed eddy accumulation (e.g., Businger & Oncley, 1990) methods. It is, however, difficult to quantify the error on the dust flux resulting from the assumption of similarity between dust and momentum (or heat) transports. The eddy diffusivity considered in the flux-gradient approach could be corrected by applying a Schmidt number similarly as a Prandtl number for the heat flux, but this Schmidt number should depend on the friction velocity. A proper comparison of the dust fluxes obtained from the eddy covariance and flux-gradient techniques will be the subject of a future study.

6. Conclusion

The partition of the near-surface dust flux in number according to the type and time scale of turbulent structures has been analyzed for the first time during the aeolian erosion of an isolated bare plot and compared with the partition of the heat and momentum fluxes. This was made possible by measuring size-resolved dust flux in number near the surface using the eddy covariance method. With this technique, we were able to capture the main eddies responsible for the net emission dust flux, confirming the potential of the eddy covariance technique for estimating dust flux close to the surface.

Contrary to the usual assumption, for moderate wind conditions and an isolated erodible plot typical of semiarid regions, dust did not appear transported similarly as momentum or heat near the surface. Although dust was mainly transported by ejection and sweep motions as heat and momentum, the partition of the dust flux between ejection and sweep motions as well as between eddy time scales was significantly different from that of momentum and heat fluxes. This was observed for all particle sizes lower than 6 μm as well as for all erosion events. Importantly, this was observed for local erosion events with net emission fluxes, that

is, emission larger than deposition. This dissimilarity would probably be lower (1) for emission events where most of the near-surface dust particles were not locally emitted such as over a very wide erodible surface and (2) for deposition events of large-scale advected dust.

This dissimilarity results from the intermittency of dust emission compared to the more continuous surface heat emission and momentum absorption. The threshold condition of dust release according to the wind intensity reduces the number of upward motions in contact with the surface transporting all together high dust concentration, warm air, and low momentum. Many upward motions transported low dust concentration with warm air and low momentum. This dissimilarity was more pronounced at large scales (several minutes time scale) due to the dominant saltation occurrence, and thus dust emission, during the passage of high-speed streaky flow structures. This dissimilarity diminishes with increasing wind speed. A rapid extrapolation of our results suggests that a similarity in turbulent transport between dust and heat-momentum could only be reached for strong erosion events with friction velocities above 2.5 to 3.0 times the threshold friction velocity.

Our findings suggest that assuming similarity between dust and momentum fluxes when estimating the dust flux, such as with the flux-gradient approach, could lead to an error, especially when saltation is not fully spatially developed. A proper comparison between dust fluxes estimated from both approaches, eddy covariance and flux gradient, is necessary to quantify this possible error.

Finally, this dissimilarity in turbulent transport of particles, heat, and momentum may hold true for other passive abiotic and biotic particles for which emission is mechanically and biologically conditioned by environmental forcing with a threshold effect as for mineral dust.

Acknowledgments
We acknowledge the support of the French National Research Agency (ANR) under the grant ANR-15-CE02-0013 (project WIND-O-V). We would like to thank (i) Houcine Khatteli, Director of the Institut des Régions Arides (IRA) of Médenine, for the constant support of IRA in all research related to wind erosion, and in particular for giving us access to the Dar Dhaoui's experimental range and for the IRA's logistic help during the all experiment to ensure the success of the campaign, (ii) the guards of the experimental stations (Noureddine Boukhli, Mokhtar Elghoul, and Mousbah Elghoul) for their constant help and surveillance of the experimental system, and (iii) Christophe Chipeaux for his help with the data-acquisition setup from Raspberry PI. Finally, we thank the three anonymous reviewers for their helpful comments. The processed data used in this study are available at the WIND-O-V Web site (https://www6.inra.fr/anr-windov/).

References

Adrian, R. J. (2007). Hairpin vortex organization in wall turbulence. *Physics of Fluids*, *19*(4), 041301. https://doi.org/10.1063/1.2717527

Alfaro, S. C., Gaudichet, A., Gomes, L., & Maillé, M. (1997). Modeling the size distribution of a soil aerosol produced by sandblasting. *Journal of Geophysical Research*, *102*(D10), 11,239–11,249.

Baas, A. C. W., & Sherman, D. J. (2005). Formation and behavior of aeolian streamers. *Journal of Geophysical Research*, *110*, F03011. https://doi.org/10.1029/2004JF000270

Bonasoni, P., Cristofanelli, P., Calzolari, F., Bonafé, U., Evangelisti, F., Stohl, A., et al. (2004). Aerosol-ozone correlations during dust transport episodes. *Atmosphere Chemical Physics*, *4*, 1201–1215.

Businger, J. A., & Oncley, S. P. (1990). Flux measurement with conditional sampling. *Journal of Atmospheric and Oceanic Technology*, *7*, 349–352.

Businger, J. A., Wyngaard, J. C., Izumi, Y., & Bradley, E. F. (1971). Flux-profile relationships in atmospheric surface layer. *Journal of the Atmospheric Sciences*, *28*(2), 181–189.

Cava, D., Katul, G. G., Sempreviva, A. M., Giostra, U., & Scrimieri, A. (2008). On the anomalous behaviour of scalar flux-variance similarity functions within the canopy sub-layer of a dense alpine forest. *Boundary-Layer Meteorology*, *128*(1), 33–57.

Damay, P. E., Maro, D., Coppalle, A., Lamaud, E., Connan, O., Hébert, D., et al. (2009). Size-resolved eddy covariance measurements of fine particle vertical fluxes. *Journal of Aerosol Science*, *40*(12), 1050–1058.

Derbyshire, E. (2007). Natural minerogenic dust and human health. *Ambio*, *36*(1), 73–77.

Deventer, M. J., El-Madany, T., Griessbaum, F., & Klemm, O. (2015). One-year measurement of size-resolved particle fluxes in an urban area. *Tellus B*, *67*(1).

Deventer, M. J., Held, A., El-Madany, T. S., & Klemm, O. (2015). Size-resolved eddy covariance fluxes of nucleation to accumulation mode aerosol particles over a coniferous forest. *Agricultural and Forest Meteorology*, *214-215*, 328–340.

Dorsey, J. R., Nemitz, E., Gallagher, M. W., Fowler, D., Williams, P. I., Bower, K. N., & Beswick, K. M. (2002). Direct measurements and parameterisation of aerosol flux, concentration and emission velocity above a city. *Atmospheric Environment*, *36*(5), 791–800.

Dupont, S., Bergametti, G., Marticorena, B., & Simoëns, S. (2013). Modeling saltation intermittency. *Journal of Geophysical Research: Atmospheres*, *118*, 1–20.

Dupont, S., & Patton, E. G. (2012). Momentum and scalar transport within a vegetation canopy following atmospheric stability and seasonal canopy changes: The CHATS experiment. *Atmosphere Chemical Physics*, *12*, 5913–5935.

Dupont, S., Rajot, J.-L., Labiadh, M., Bergametti, G., Alfaro, S., Bouet, C., et al. (2018). Aerodynamic parameters over an eroding bare surface: Reconciliation of the law-of-the-wall and eddy-covariance determinations. *Journal of Geophysical Research: Atmospheres*, *123*, 4490–4508. https://doi.org/10.1029/2017JD027984

Foken, T., Göockede, M., Mauder, M., Mahrt, L., Amiro, B. D., & Munger, J. W. (2004). Post-field data quality control. In X. Lee (Ed.), *Handbook of micrometeorology: A guide for surface flux measurements*. Netherlands: 2004 Kluwer Academic Publishers.

Fratini, G., Ciccioli, P., Febo, A., Forgione, A., & Valentini, R. (2007). Size-segregated fluxes of mineral dust from a desert area of northern China by eddy covariance. *Atmospheric Chemistry and Physics*, *7*(11), 2839–2854.

Fryrear, D. W. (1986). A field dust sampler. *Journal of Soil and Water Conservation*, *41*(2), 117–120.

Gillette, D. A., Blifford, Jr. I. H., & Fenster, C. R. (1972). Measurements of aerosol size distributions and vertical fluxes of aerosols on land subject to wind erosion. *Journal of Applied Meteorology*, *11*, 977–987.

Gillette, D. A., & Porch, W. M. (1978). The role of fluctuations of vertical and horizontal wind and particle concentration in the deposition of dust suspended by wind. *Journal of Geophysical Research*, *83*(C1), 409–414.

Gomes, L., Bergametti, G., Coudé-Gaussen, G., & Rognon, P. (1990). Submicron desert dusts: A sandblasting process. *Journal of Geophysical Research*, *95*(D9), 13,927–13,935.

Howell, J. F., & Mahrt, L. (1997). Multiresolution flux decomposition. *Boundary-Layer Meteorology*, *83*, 117–137.
Hutchins, N., Chauhan, K., Marusic, I., Monty, J., & Klewicki, J. (2012). Towards reconciling the large-scale structure of turbulent boundary layers in the atmosphere and laboratory. *Boundary-Layer Meteorology*, *145*(2), 273–306.
IPCC (2013). Climate change: The physical science basis. In T. F. Stocker et al. (Eds.), *Contribution of Working Group I to the Fifth Assessment Report of the Intergovernmental Panel on Climate Change* (pp. 2013). Cambridge: Cambridge University Press.
Ishizuka, M., Mikami, M., Leys, J. F., Shao, Y., Yamada, Y., & Heidenreich, S. (2014). Power law relation between size-resolved vertical dust flux and friction velocity measured in a fallow wheat field. *Aeolian Research*, *12*, 87–99.
Kaimal, J. C., & Finnigan, J. J. (1994). *Atmospheric boundary layer flows. Their structure and measurements*, pp. 289. New York: Oxford University Press.
Kaimal, J. C., Wyngaard, J. C., Izumi, Y., & Coté, O. R. (1972). Spectral characteristics of surface-layer turbulence. *Quarterly Journal of the Royal Meteorological Society*, *98*, 563–589.
Katul, G., Goltz, S. M., Hsieh, C. I., Cheng, Y., Mowry, F., & Sigmon, J. (1995). Estimation of surface heat and momentum fluxes using the flux-variance method above uniform and non-uniform terrain. *Boundary-Layer Meteorology*, *74*(3), 237–260.
Katul, G., Kuhn, G., Schieldge, J., & Hsieh, C. I. (1997). The ejection-sweep character of scalar fluxes in the unstable surface layer. *Boundary-Layer Meteorology*, *83*, 1–26.
Katul, G. G., Sempreviva, A. M., & Cava, D. (2008). The temperature-humidity covariance in the marine surface layer: A one-dimensional analytical model. *Boundary-Layer Meteorology*, *126*(2), 263–278.
Kays, W. M. (1994). Turbulent Prandtl number—Where are we? *Journal of Heat Transfer*, *116*(2), 284–295.
Lamaud, E., & Irvine, M. (2006). Temperature-humidity dissimilarity and heat-to-water-vapour transport efficiency above and within a pine forest canopy: The role of the Bowen ratio. *Boundary-Layer Meteorology*, *120*(1), 87–109.
Lettau, K., & Lettau, H. (1978). *Experimental and Micro-meteorological field studies of dune migration*, vol. Exploring the World's Driest Climate (pp. 110–147). Madison: Inst. for Environ. Stud., Univ. of Wisc.
Li, D., & Bou-Zeid, E. (2011). Coherent structures and the dissimilarity of turbulent transport of momentum and scalars in the unstable atmospheric surface layer. *Boundary-Layer Meteorology*, *140*(2), 243–262.
Liu, D., Ishizuka, M., Mikami, M., & Shao, Y. (2018). Turbulent characteristics of saltation and uncertainty of saltation model parameters. *Atmospheric Chemistry and Physics*, *18*, 7595–7606.
Mahowald, N. (2011). Aerosol indirect effect on biogeochemical cycles and climate. *Science*, *334*(6057), 794–796.
Mårtensson, E. M., Nilsson, E. D., Buzorius, G., & Johansson, C. (2006). Eddy covariance measurements and parameterisation of traffic related particle emissions in an urban environment. *Atmospheric Chemistry & Physics*, *6*, 769–785.
Moene, A. F., Michels, B. I., & Holtslag, A. A. M. (2006). Scaling variances of scalars in a convective boundary layer under different entrainment regimes. *Boundary-Layer Meteorology*, *120*, 257–274.
Neakrase, L. D. V., Balme, M. R., Esposito, F., Kelling, T., Klose, M., Kok, J. F., et al. (2016). Particle lifting processes in dust devils. *Space Science Reviews*, *203*, 347–376.
Nickling, W. G., & Gillies, J. A. (1993). Dust emission and transport in Mali, West Africa. *Sedimentology*, *40*, 859–868.
Nilsson, E. O., Sahlée, E., & Rutgersson, A. (2014). Turbulent momentum flux characterization using extended multiresolution analysis. *Quarterly Journal of the Royal Meteorological Society*, *140*, 1715–1728.
Oncley, S. P., Friehe, C. A., Larue, J. C., Businger, J. A., Itsweire, E. C., & Chang, S. S. (1996). Surface-layer fluxes, profiles, and turbulence measurements over uniform terrain under near-neutral conditions. *Journal Atmospheric Sciences*, *53*(7), 1029–1044.
Pierre, C., Kergoat, L., Hiernaux, P., Baron, C., Bergametti, G., Rajot, J. L., et al. (2018). Impact of agropastoral management on wind erosion in Sahelian croplands. *Land Degradation and Development*, *29*, 800–811.
Porch, W. M., & Gillette, D. A. (1977). A comparison of aerosol and momentum mixing in dust storms using fast-response instruments. *Journal of Applied Meteorology*, *16*, 1273–1281.
Robinson, S. K. (1991). Coherent motions in the turbulent boundary-layer. *Annual Review of Fluid Mechanics*, *23*, 601–639.
Salesky, S. T., Chamecki, M., & Bou-Zeid, E. (2017). On the nature of the transition between roll and cellular organization in the convective boundary layer. *Boundary-Layer Meteorology*, *163*, 41–68.
Shao, Y. (2008). *Physics and modelling of wind erosion*, 2nd revised and expanded edition (pp. 467). Berlin, Germany: Springer.
Shao, Y., Ishizuka, M., Mikami, M., & Leys, J. F. (2011). Parameterization of size-resolved dust emission and validation with measurements. *Journal of Geophysical Research*, *116*, D08203. https://doi.org/10.1029/2010JD014527
Shao, Y., Wyrwoll, K.-H., Chappell, A., Huang, J., Lin, Z., McTainsh, G. H., et al. (2011). Dust cycle: An emerging core theme in Earth system science. *Aeolian Research*, *2*(4), 181–204.
Sow, M., Alfaro, S. C., Rajot, J. L., & Marticorena, B. (2009). Size resolved dust emission fluxes measured in Niger during 3 dust storms of the AMMA experiment. *Atmosphere Chemical Physics*, *9*(12), 3881–3891.
Stull, R. B. (1988). *An introduction to boundary layer meteorology* (pp. 666). Dordrecht, The Netherlands: Kluwer Academic Pub.
Townsend, A. A. (1976). The structure of turbulent shear flow, Cambridge.
Vickers, D., & Mahrt, L. (2003). The cospectral gap and turbulent flux calculations. *Journal of Atmospheric and Oceanic Technology*, *20*, 660–672.
Vinkovic, I., Doppler, D., Lelouvetel, J., & Buffat, M. (2011). Direct numerical simulation of particle interaction with ejections in turbulent channel flows. *International Journal of Multiphase Flow*, *37*(2), 187–197.
Wang, G., Zheng, X., & Tao, J. (2017). Very large scale motion and PM10 concentration in a high-Re boundary layer. *Physical Fluids*, *29*, 61701.
Warhaft, Z. (2000). Passive scalars in turbulent flows. *Annual Review of Fluid Mechanics*, *32*, 203–240.
Williams, C. A., Scanlon, T. M., & Albertson, J. D. (2007). Influence of surface heterogeneity on scalar dissimilarity in the roughness sublayer. *Boundary-Layer Meteorology*, *122*, 149–165.
Yin, Y., Wurzler, S., Levin, Z., & Reisin, T. G. (2002). Interactions of mineral dust particles and clouds: Effects on precipitation and cloud optical properties. *Journal of Geophysical Research*, *107*, D234724. https://doi.org/10.1029/2001JD001544
Yu, H., Chin, M., Yuan, T., Bian, H., Remer, L. A., Prospero, J. M., et al. (2015). The fertilizing role of African dust in the Amazon rainforest: A first multiyear assessment based on data from cloud-aerosol lidar and infrared pathfinder satellite observations. *Geophysical Research Letters*, *42*, 1984–1991.